

THE REDDEST DR3 SDSS/XMM-NEWTON QUASARS

M. YOUNG^{1,2}, M. ELVIS¹, G. RISALITI^{1,3}

Draft version November 4, 2018

ABSTRACT

We have cross-correlated the SDSS DR3 Schneider et al. (2005) quasar catalog with the XMM-Newton archive. Color and redshift selections ($g - r \geq 0.5$ and $0.9 < z < 2.1$) result in a sample of 17 red, moderate redshift quasars. The redshift selection minimizes possible contamination due to host galaxy emission and Ly α forest absorption. Both optical and X-ray information are required to distinguish between the two likely remaining causes of the red colors: 1) dust-reddening and 2) an intrinsically red continuum. We find that 7 of 17 quasars can be classified as probable ‘intrinsically red’ objects. These 7 quasars have unusually broad MgII emission lines ($\langle \text{FWHM} \rangle = 10,500 \text{ km s}^{-1}$), moderately flat, but unabsorbed X-ray spectra ($\langle \Gamma \rangle = 1.66 \pm 0.08$), and low accretion rates ($\dot{M}/\dot{M}_{\text{Edd}} \sim 0.01$). We suggest low accretion rates as a possible physical explanation for quasars with intrinsically red optical continua. We find that 8 of 17 quasars can be classified as dust-reddened. Three of these have upper-limits on the absorption column from X-ray spectral fits of $N_{\text{H}} = 3\text{--}13 \times 10^{22} \text{ cm}^2$, while the other five quasars must be absorbed by at least $N_{\text{H}} = 10^{23} \text{ cm}^2$ in order to be consistent with a comparably selected $\alpha_{\text{ox}} - l_{\text{uv}}$ distribution. Two objects in the sample are unclassified.

Subject headings: accretion disks — galaxies: active — quasars: general

1. INTRODUCTION

Until recently, quasars have typically been selected as point-like objects with colors bluer than stars (e.g. $U - B < -0.44$, Schmidt & Green 1983). This limited the possible spectral energy diagrams (SEDs) that known quasars could have. A composite SED shows that quasars’ blue colors are due to the Big Blue Bump (BBB) continuum feature that dominates the optical and UV spectrum (Malkan & Sargent 1982; Elvis et al. 1994). However, surveys using different selection mechanisms discovered that quasars can have red colors as well, indicating a diminished or missing BBB. While in many cases, this reddening is due to dust obscuration, some cases may be due to changes in the accretion disk thought to power the optical/UV continuum. We identify such a population in this paper.

Red quasars were first discovered in the Webster et al. (1995) sample of radio-loud quasars. Webster et al. (1995) suggested dust-reddening as the cause of the red $B_J - K$ colors and estimated that red colors could cause as much as 80% of the quasar population to go undetected in existing optical surveys. Some 200 members of a new population of red, radio-quiet quasars were discovered in the near-infrared (1-2 μm) with the Two Micron All Sky Survey (2MASS) by Cutri et al. (2002). The space density of the red 2MASS quasars was found to be at least equal to that of optical and UV-selected quasars. Cutri et al. (2002) also suggested dust-reddening to explain the red colors of the 2MASS red quasars because the near-IR color distribution is consistent with a reddening of $A_V = 1\text{--}5$ magnitudes. In addition, $\sim 10\%$ of the predominantly radio-quiet sample is highly polarized

($P > 3\%$) (Smith et al. 2002). Supporting this conclusion, Chandra and XMM-Newton observations of red 2MASS AGN find spectra that are either unusually hard or absorbed by $N_{\text{H}} = 10^{21}\text{--}10^{23} \text{ cm}^{-2}$ (Wilkes et al. 2002, 2005; Urrutia et al. 2005).

Unlike UV-excess based surveys, the Sloan Digital Sky Survey (SDSS) allows detection of red quasars in the optical band because the algorithm for selecting candidates for spectroscopy uses a four-dimensional multicolor selection criterion (Richards et al. 2003) similar to that of the 2dF QSO Redshift Survey (Croom et al. 2004). This allows the SDSS to select all objects lying outside of the stellar locus, including atypically red quasars. Richards et al. (2003) explored the color distribution of SDSS quasars and found that while a population of intrinsically red quasars exists, the majority of the red tail of the color distribution is explained by dust reddening. In a later study (Hopkins et al. 2004), the curvatures of the SDSS spectra were found to be best-fit by a dust extinction curve similar to that of the Small Magellanic Cloud (SMC) (Prevot et al. 1984). However, only mildly dust-reddened quasars can be detected ($E(B-V) < 0.5$) in the SDSS before dust extinction causes them to drop below the detection threshold of the survey (Richards et al. 2003).

While dust-reddening is a common explanation for red colors in quasars, other possible explanations include: (1) host galaxy contamination, (2) absorption by the Ly α forest, (3) optical synchrotron emission superimposed on a normal, blue spectrum to create a red spectrum (Serjeant & Rawlings 1996; Francis et al. 2000; Whiting et al. 2001), and (4) an intrinsically red continuum. The redshift selection in this paper minimizes contamination via options (1) and (2).

X-ray observations used in conjunction with optical information can constrain the amount of intrinsic absorption in a source, thereby allowing an investigation of dust-reddened versus intrinsically red optical continua.

Electronic address: myoung@cfa.harvard.edu

¹ Harvard-Smithsonian Center for Astrophysics, 60 Garden St. Cambridge, MA 02138 USA

² Boston University, Astronomy Department, 725 Commonwealth Ave., Boston, MA 02215

³ INAF - Osservatorio di Arcetri, Largo E. Fermi 5, Firenze, Italy

Previous studies have found intrinsically red quasar candidates in addition to dust-reddened quasars. For example, Hall et al. (2006) selected a sample of 12 red quasars from the SDSS, but Chandra X-ray observations show evidence for NH absorption ($N_H \sim 10^{22} \text{ cm}^{-2}$) for only 4 of their 12 quasars. The other seven quasars show no evidence for even moderate intrinsic absorption and three of these show evidence for an intrinsically red optical continuum.

In a similar vein, Risaliti et al. (2003) observed 16 optically-selected, X-ray weak quasars with Chandra. While the sample was not selected to be red, the average color of the sample is redder than that of the parent Hamburg Quasar Survey ($\Delta(B-R) \sim 1$ vs. $\Delta(B-R) \sim 0.5$). The X-ray weak quasars have a flat average photon index, $\langle \Gamma \rangle = 1.5$ (where $\Gamma = -\alpha + 1$ for $F_\nu \propto \nu^\alpha$) and 12 of the 16 quasars have steeper optical-to-X-ray indices than normal. (The optical-to-X-ray continuum is characterized by $\alpha_{ox} = \log(F_{2\text{keV}}/F_{uv}) / \log(\nu_{2\text{keV}}/\nu_{uv})$, where $F_{2\text{keV}}$ and F_{uv} are the intrinsic flux densities at 2 keV and 2500 Å, respectively (Tananbaum et al. 1979).) While X-ray absorption remains a possibility, Risaliti et al. (2003) argue that these quasars are intrinsically underluminous in the X-rays. The evidence, however, is not conclusive due to the low signal-to-noise for many of the Chandra spectra.

Larger surveys including high quality optical and X-ray spectra are now possible with the advent of the SDSS and the XMM-Newton archive of X-ray observations, both of which cover large areas of the sky. SDSS data can constrain dust-reddening in the optical, while XMM-Newton observations constrain absorption in the X-rays. In this paper we investigate the optical and X-ray properties of 17 red SDSS quasars. §2 introduces the data sources and sample selection and §3 covers the optical and X-ray reduction and data analysis. In §4, we classify the quasars as dust-reddened, intrinsically red or unclassified, and in §5 we discuss low accretion rates as a possible explanation for the steep optical/UV spectra of intrinsically red quasars. We assume throughout the paper that $H_0 = 70 \text{ km s}^{-1} \text{ Mpc}^{-1}$, $\Omega_M = 0.3$, and $\Omega_\Lambda = 0.7$.

2. SAMPLE SELECTION

2.1. Data Sources: SDSS & XMM Newton

The third version of the SDSS quasar catalog (Schneider et al. 2005) is based on Data Release 3 (DR3), which covers an area of 5,282 deg² (Abazajian et al. 2005). The quasar catalog contains 46,240 objects from the SDSS that have: (1) $15.0 < i < 22.2$; (2) $M_i < -22.0$; (3) at least one emission line with FWHM greater than 1000 km s⁻¹, or (4) unambiguous broad absorption line characteristics. SDSS photometry in the u , g , r , i and z bands covers 3,250 - 10,000 Å. SDSS spectroscopy covers 3,800 - 9,200 Å (so the u band and part of the z band lie outside the spectral range), with a spectral resolving power of $\sim 2,000$.

The SDSS DR3 quasar catalog overlaps with 1% of the area of archival XMM-Newton observations. XMM-Newton imaging is carried out by the three European Photon Imaging Cameras (EPIC): MOS-1, MOS-2, and pn (Turner et al. 2001; Strueder et al. 2001). The XMM-Newton telescope is good for retrieving serendipitous X-ray spectra of SDSS quasars due to a large collecting area

(922 cm² for MOS and 1,227 cm² for PN at 1 keV), large field of view (33' x 33' for MOS and 27.5' x 27.5' for PN), and good spectral resolution ($E/\Delta E \sim 20 - 50$ for both MOS and PN)⁴. The XMM-Newton spectral range covers the 0.5 - 12 keV band.

The SDSS and XMM-Newton archives are well-matched in sensitivity. A source with a 2-10 keV flux of $10^{-14} \text{ erg s}^{-1} \text{ cm}^{-2}$ and a standard radio quiet spectrum ($\Gamma \sim 2.0$) produces ~ 100 counts in ~ 10 ksec, sufficient for a crude spectral fit. For a typical value of $\alpha_{ox} = -1.5$ (Vignali et al. 2003), a $10^{-14} \text{ ergs cm}^{-2} \text{ s}^{-1}$ quasar would have $r = 19.37$ while an X-ray quiet quasar with $\alpha_{ox} = -2.0$ would have $r = 15.63$. Both of these magnitudes lie comfortably in the SDSS range.

2.2. The SDSS-XMM Red Quasar Sample

We define our red sample of Schneider et al. (2005) quasars lying in XMM-Newton fields by selecting the most extreme red colors, $g - r \geq 0.5$. By further restricting our search to moderate redshifts ($0.9 < z < 2.1$), we minimize host galaxy contribution at low redshifts ($z < 0.5$) and Ly α forest absorption at high redshifts ($z > 2.5$). This selection results in a sample of 17 quasars.

Richards et al. (2003), hereafter R03, defines dust-reddened quasars via their relative colors. Relative colors compare a quasar's measured colors with the median colors in its redshift bin, where redshift bin sizes are 0.1 in redshift, so that $\Delta(g - i) = (g - i) - \langle (g - i) \rangle_z$. The use of relative colors corrects for the effect of typical emission lines on the photometry in a particular band. The relative colors of the SDSS quasars match a Gaussian distribution on the blue side but require the addition of a tail on the red side (Fig. 3 in R03). R03 identifies quasars belonging to the red tail as $\Delta(g - i) > 0.2$, since the $\Delta(g - i)$ color correlates best with the photometric spectral index. The $\Delta(g - i)$ color has been corrected for an SMC-like extinction curve with $E(B - V) = 0.04$, a value typical of high Galactic latitudes, for which $E(g - i) = 0.07$. In practice, this yields a minimum of $\Delta(g - i) \sim 0.35$ for the quasars with redshift $z \sim 1.5$. The $(g - i)$ and $(g - r)$ colors behave similarly with redshift (Fig. 2 of R03), and the maximum median color is 0.2 for $1 < z < 2$. In Figure 1, we show a histogram of the relative $(g - i)$ colors for our sample. Only two have $\Delta(g - i) < 0.35$. Thus, the $g - r \geq 0.5$ color selection mimics $\Delta(g - i) > 0.35$, though we do not use relative colors.

Our red quasar sample is unbiased in X-ray loudness since we do not require X-ray detections for selection. Nevertheless, the X-ray detection rates are high: 94% for 2σ detections (16/17) and 76% for $> 3\sigma$ detections (13/17), although most of the quasars have a relatively low X-ray signal-to-noise: 10/17 quasars have $S/N < 10$.

Table 1 lists the sample, giving the source ID number used within this paper, the full SDSS name, radio classification, X-ray S/N (which is averaged if multiple observations are available), redshift, Galactic N_H , and the absolute i -band magnitude M_i . A source is radio loud if $F_{5\text{GHz}} / F_{4400} = R_L > 10$ (Kellerman et al. 1989). To calculate R_L , a power-law is interpolated between the optical magnitudes to get $F_\lambda(4400)$, and the 1.4 GHz radio

⁴ http://imagine.gsfc.nasa.gov/docs/sats_n_data/missions/xmm.html

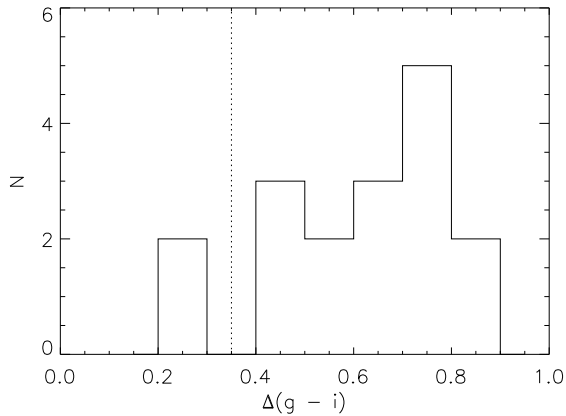


FIG. 1.— The $\Delta(g - i)$ color distribution of the red sample. The majority of sources in this sample meet the Richards et al. (2003) requirement that $\Delta(g - i) > 0.35$ for dust-reddened quasars.

flux is obtained from FIRST survey detections (White et al. 1997), which are extrapolated to 5 GHz using a radio power-law $\alpha_R = -0.8$. All the quasars lie in the area covered by the FIRST survey, so if there is no detection, we use the 5σ upper-limit on the 1.4GHz radio flux to extrapolate to 5 GHz.

For five of 17 sources, there are two X-ray observations. In these cases, both observations were processed and used in our analysis.

2.3. SDSS Data

SDSS photometry was extracted from the online database⁵ via SQL-based queries in CasJobs. The individual, calibrated SDSS spectra were also downloaded from the SDSS database. Table 2 gives the source ID, the abbreviated SDSS name, the $g - r$ color (which determined selection), the apparent i band magnitude, and the full-width half-maximum (FWHM [km s^{-1}]) of the broad MgII component. The MgII information is taken from Shen et al. (2007) for all but three objects. Shen et al. (2007) simultaneously fit the FeII emission, a continuum power-law, and broad and narrow Gaussians to the MgII line. The spectral signal-to-noise is too low for two objects (#13 and #15) to use this method. Another object (#17) has good S/N, but line values are not given in Shen et al. (2007). We fit the MgII lines for these three sources by estimating the continuum values by eye and then simultaneously fitting broad and narrow Gaussians with IRAF⁶.

There is one broad-absorption line quasar (BAL) in the sample, SDSS J0944+0410 (#1), and two narrow absorption-line (NAL) quasars, SDSS J1226+0130 (#8) and SDSS J1435+4851 (#9). Only five of the 17 quasars have the CIV line, which is the most reliable marker of BAL/NAL presence, visible in their spectra. MgII, the BEL seen in all 17 quasars, rarely shows either BALs or NALs. So the true number of BALs and NALs in the sample could be even greater.

2.4. X-ray Data Reduction

Using the XMM-Newton Science Analysis System, SAS v7.02⁷, we filtered the XMM observations to remove

time intervals of flaring high-energy background events using the standard cut-off of 0.35 cts s^{-1} for the MOS cameras and 1.0 ct s^{-1} for the PN camera. The event rate plots were visually examined to determine that these cut-offs were appropriate. We then extracted source and background regions for spectral analysis. The SAS task *eregionanalyse* was used to select the source radius with the optimal signal-to-noise, with typical radii ranging from $10''$ to $60''$. Background regions were defined by eye, avoiding obvious X-ray sources and chip edges. These regions were typically a circle of radius 2000-2500 pixels (100 - $125''$), selected to lie on the same chip as the source and as close to the source as possible without overlapping the source extraction region.

Where possible, observations were retrieved for all three XMM EPIC CCDs. In seven observations, the source lies in a bad region in one of the cameras, either in a strip between two chips or, because the MOS and PN cameras have different shapes, the source may lie outside the field of view in one of the cameras. In an eighth case, the source is within the field of view of all three cameras, but in the MOS-2 camera, most of the events are filtered out while removing the flaring high-energy background. In all these cases (7 of 22 observations), we use the remaining images from the other cameras for analysis.

Table 3 contains data for the XMM observations, ordered by increasing S/N. The table includes the source ID, XMM identification number, observation date, net exposure time, net counts, X-ray S/N and the cameras available for analysis.

3. ANALYSIS

3.1. Optical Spectra and Continuum Dust Reddening Fits

We wrote an IDL procedure to fit dust-reddening to the optical continuum. The procedure calls a de-reddening routine, FM_UNRED.PRO (Landsman 1999), which uses the Fitzpatrick (1999) parameterization to characterize the optical and UV extinction curve.

Each source spectrum is first shifted to the rest-frame. A composite quasar spectrum created from SDSS quasars (Vanden Berk et al. 2001) is then reddened incrementally with the SMC extinction curve (Gordon et al. 2003) and normalized to the red quasar spectrum by averaging the continuum between 3020 and 3066 Å (Vanden Berk et al. 2001) in order to calculate the χ^2 value. The best-fit parameters are those for which χ^2 reached a minimum. The total χ^2 was allowed to vary by 2.7 to get the 90% confidence interval errors.

The SMC, rather than Galactic, extinction curve is used because of the absence of the $\lambda 2175$ feature in AGN spectra (Pitman et al. 2000; Kuhn et al. 2001; Czerny et al. 2004; Hopkins et al. 2004). The optical dust-reddening (hereafter denoted as $E(B-V)_{\text{spec}}$) is allowed to vary from $E(B-V)_{\text{spec}} = 0.0$ to $E(B-V)_{\text{spec}} = 1.0$. Simulations have shown that quasars with $E(B-V) > 0.5$ are not expected from the SDSS selection process (Richards et al. 2003), so the fits to the spectral continuum cover the full $E(B-V)$ parameter space.

The Small Blue Bump, a blend of Balmer continuum emission and FeII lines, extends from $\sim 2000 - 4000 \text{ \AA}$ (Wills, Netzer & Wills 1985). Our color selection criteria ($g - r \geq 0.5$) bias our sample towards sources with

⁵ <http://www.sdss.org/dr3/access/index.html>

⁶ <http://iraf.noao.edu/>

⁷ <http://xmm.esac.esa.int/sas>

TABLE 1
SDSS/XMM-NEWTON RED QUASAR SAMPLE

Source ID	SDSS name	R_L^a	$(S/N)_x^b$	z	$N_{H,gal}$ (10^{20} cm^{-2})	M_i
1	SDSS J094440.43+041055.5	RQ	0.17	1.98	3.63	-25.3
2	SDSS J023217.68-073119.9	RQ	3.23	1.16	3.05	-23.6
3	SDSS J165245.77+394722.3	RQ	1.89	1.19	1.64	-24.2
4	SDSS J072843.03+370835.0	RL ($R_L = 34.8$)	2.87	1.40	6.00	-24.0
5	SDSS J100201.50+020329.4	RQ	2.85	2.01	2.59	-25.0
6	SDSS J221723.29-082139.4	RQ	2.93	1.25	5.30	-24.2
7	SDSS J153322.80+324351.4	RQ	4.04	1.90	2.05	-24.8
8	SDSS J122637.01+013016.1	RQ	4.69	1.55	1.84	-25.2
9	SDSS J143513.89+484149.3	RQ	4.46	1.89	2.07	-24.7
10	SDSS J221719.55-081234.4	RQ	5.88	1.46	5.31	-24.1
11	SDSS J111452.84+531531.7	RQ	6.33	1.21	0.923	-24.1
12	SDSS J113342.73+490025.8	RQ	8.65	1.30	1.59	-24.6
13	SDSS J125456.82+564941.4	($R_L < 18.3$)	14.43	1.27	1.26	-22.8
14	SDSS J095918.70+020951.4	RL ($R_L = 36.3$)	21.87	1.16	2.64	-23.4
15	SDSS J095857.34+021314.4	RQ	27.94	1.02	2.64	-23.0
16	SDSS J105316.76+573550.7	RQ	35.21	1.21	0.556	-23.9
17	SDSS J091301.01+525928.9	RQ ($R_L = 4.9$)	43.48	1.38	1.60	-26.9

^aThe radio loud parameter R_L is defined as F_{5GHz}/F_{4400} , where $R_L > 10$ indicates radio-loudness (Kellerman et al. 1989).

^bWhen more than one X-ray observation exists for a single source, the S/N listed is the rms of the observations.

TABLE 2
RED QUASAR SAMPLE IN THE SDSS

ID	SDSS name	g - r	i	MgII FWHM (km s^{-1})
1	SDSS J0944+0410	0.50	18.22	8,800
2	SDSS J0232-0731	0.53	19.25	11,700
3	SDSS J1652+3947	0.54	18.65	8,800
4	SDSS J0728+3708	0.74	19.09	9,700
5	SDSS J1002+0203	0.55	18.58	10,800
6	SDSS J2217-0821	0.74	18.69	7,600
7	SDSS J1533+3243	0.97	18.69	6,700
8	SDSS J1226+0130	0.59	18.01	7,700
9	SDSS J1435+4841	0.50	18.78	7,000
10	SDSS J2217-0812	0.62	19.06	5,800
11	SDSS J1114+5315	0.76	18.77	6,400
12	SDSS J1133+4900	0.52	18.42	9,100
13	SDSS J1254+5649 ^a	0.57	20.12	8,200
14	SDSS J0959+0209	0.60	19.40	23,200
15	SDSS J0958+0213 ^a	0.59	19.66	10,500
16	SDSS J1053+5735	0.55	18.95	5,400
17	SDSS J0913+5259 ^a	0.64	16.20	6,000

NOTE. — FWHM measurements for the MgII broad emission lines are from Shen et al. (2007).

^aThe line parameters for these sources are not included in Shen et al. (2007). Instead, broad and narrow Gaussians were fit simultaneously to the line, with the continuum estimated by eye. The FWHM for broad Gaussian component are listed.

atypically large FeII emission between $\sim 2200 - 2700 \text{ \AA}$. Five of 17 sources have atypical FeII emission. Excluding the region from 2200 - 3000 \AA from the chi-square calculation for all the sources accounts for both FeII emission and the 2798 \AA MgII line, so that the reddening fit to the continuum is not biased by unusually strong line emission. The reddening fit was not sensitive to other broad emission lines, such as the 1549 \AA CIV line, so we did not omit any additional lines from the fit. The BAL quasar (SDSS J0944+0410, #1) was not fit with reddening because numerous absorption lines and a strong Fe II bump left no reliable continuum points with which to calculate χ^2 .

We also fit a power-law ($F_\nu \propto \nu^{\alpha_{opt}}$) to the optical continuum. All major emission lines are removed before

performing the fit, as is the region dominated by the blended FeII and Balmer emission. A power-law will not be a good fit to spectral continua with obvious dust curvature, but for $(E(B-V))_{spec} < 0.1$, dust-reddening will look similar to a red power-law. Section §3.2 discusses this issue in more detail.

Figure 2 plots the SDSS source spectra in F_λ ($10^{-17} \text{ ergs cm}^{-2} \text{ s}^{-1} \text{ \AA}^{-1}$) vs. λ (\AA) space. Overplotted are the original Vanden Berk et al. (2001) template (dotted blue line), the reddened template (dashed red line), and the optical power-law (solid green line). Table 4 gives the reddening results: $E(B-V)_{spec}$, the expected intrinsic gas column density ($N_{H,opt}$) obtained by applying the Galactic gas-to-dust ratio (Bohlin et al. 1978; Kent et al. 1991), the intrinsic gas column density from the X-ray fits ($N_{H,x}$, see §3.3), and the optical power-law index, α_{opt} .

Reddening fits to the optical spectra require $E(B-V)_{spec}$ in 14 out of 17 sources at $> 3\sigma$. For these 14 sources, $E(B-V)_{spec}$ ranges from 0.04 to 0.25, with a weighted mean of $\langle E(B-V)_{spec} \rangle = 0.1$ corresponding to $\langle N_{H,opt} \rangle = 5.8 \times 10^{20} \text{ cm}^{-2}$, using the Galactic gas-to-dust ratio.

3.2. Testing the Optical Continuum for Weak Curvature with Relative Colors

We find that reddening is a good fit to most of the optical spectra. However, for the redshifts of this sample ($z > 1$), the optical continuum will not have strong dust-induced curvature for mild reddening ($E(B-V)_{spec} \leq 0.1$). Under these conditions, a dust-reddened optical continuum will look similar to a red power-law. Figure 2 in this paper shows the similarity between mild dust-reddening (dashed red line) and a red power-law (solid green line). The curvature in the relative broad-band photometry can help differentiate these two possibilities because the u band (for which the FWHM ranges from 3251 to 3851 \AA) is mostly outside the spectral range (3800 - 9200 \AA). The u band is a factor 3.6 more absorbed by dust (for $E(B-V) = 0.1$) than the r band, where the spectra are centered.

TABLE 3
XMM-NEWTON OBSERVATION LOG

Source ID	XMM ID	Date	Net Exp Time ^a (ks)	Net Counts ^a (counts)	S/N	Cameras PN M1 M2
1	0201290301	2005-6-09	56.7	0.03	0.2	- X X
2	0200730401	2005-1-30	122.8	40.3	3.2	X X X
3a	0113060401	2002-07-14	4.55	7.3	1.2	- X X
3b	0113060201	2003-9-03	5.0	19.2	2.6	- X X
4	0145450501	2003-12-04	9.2	25.1	2.9	X X X
5a	0203360401	2005-12-10	29.6	39.0	2.8	X X X
5b	0203360801	2005-12-07	89.4	11.8	2.9	X X -
6	0009650201	2002-9-20	40.2	31.2	2.9	- X X
7	0039140101	2003-8-29	25.3	70.8	4.0	X X X
8	0110990201	2002-8-11	32.3	70.3	4.7	X X X
9a	0110930401	2004-2-04	21.1	77.5	4.2	X X X
9b	0110930901	2004-2-04	17.7	98.3	4.7	X X X
10	0009650201	2002-9-20	40.2	84.5	5.9	- X X
11	0143650901	2004-5-20	17.1	135.3	6.3	X X X
12	0149900201	2004-12-15	36.0	196.3	8.7	- X X
13	0081340201	2002-11-02	60.1	750.0	14.4	X X X
14	0203361801	2005-1-16	79.3	1486.8	21.9	X X X
15	0203361801	2005-1-16	79.	2696.2	27.9	X X X
16a	0147511701	2004-2-01	282.4	4185.3	33.7	X X X
16b	0147511801	2004-2-01	282.2	4775.3	36.8	X X X
17a	0143150301	2004-9-06	20.8	3687.3	33.6	X X X
17b	0143150601	2004-9-06	47.9	9130.1	53.4	X X X

^aNet exposure time and net counts include information from all available observations. Net counts are taken from 0.5-10 keV.

TABLE 4
OPTICAL REDDENING FITS

ID	E(B-V) _{spec}	$N_{H,opt}^a$ (10^{20} cm ⁻²)	$N_{H,x}^b$ (10^{20} cm ⁻²)	α_{opt}^c
1	- ^d	-	-	-1.49
2	0.03±0.02	1.7±1.2	-	-0.92
3	0.08±0.02	4.6±1.2	-	-1.05
4	0.25±0.02	14.5±1.2	-	-2.92
5	0.052±0.005	3.0±0.3	-	-1.36
6	0.17±0.02	9.9±1.2	-	-1.95
7	0.12±0.02	7.0±1.2	≤696	-1.85
8	0.15±0.01	8.7±0.6	≤1340	-1.79
9	0.13±0.01	7.5±0.6	≤677	-2.07
10	0.11±0.02	6.4±1.2	≤184	-1.68
11	0.18±0.03	10.4±1.7	≤89.0	-1.46
12	0.04±0.01	2.3±0.6	≤76.3	-0.87
13	0.10 ^{+0.11} _{-0.08}	5.8 ^{+6.4} _{-4.6}	≤23.1	-1.44
14	0.12±0.03	7.0±1.7	≤5.49	-1.05
15	0.16 ^{+0.09} _{-0.07}	9.3 ^{+5.2} _{-4.1}	≤5.39	-1.94
16	0.11±0.02	6.4±1.2	≤4.7	-1.17
17	0.086 ^{+0.004} _{-0.003}	5.00 ^{+0.23} _{-0.17}	≤2.9	-1.31

^aGas column predicted from E(B-V)_{spec} using the Galactic gas-to-dust ratio (Bohlin et al. 1978; Kent et al. 1991).

^bGas column upper-limit measured via X-ray spectral fits (model D).

^cThe optical slope as fit to the spectral continuum with emission lines removed.

^dThe BAL quasar was not fit with E(B-V)_{spec} because numerous absorption lines made it impractical to fit using chi-square minimization.

Relative colors give an idea of the shape of the continuum (Hall et al. 2006). A quasar with a typical $g-i$ color, for example, will have $\Delta(g-i) = 0$, while a quasar with red ($g-i$) color will have $\Delta(g-i) > 0$. A dust-reddened quasar with typical emission lines will have $\Delta(u-r) > \Delta(g-i) > \Delta(r-z)$, because curvature increases on the blue side of the continuum. A typical blue power-law continuum, on the other hand, will have $\Delta(u-r) \sim \Delta(g-i) \sim \Delta(r-z)$. In the case of a power-law continuum that is redder than average, the relative colors

will go as $\Delta(u-r) < \Delta(g-i) > \Delta(r-z)$. Therefore, an object with $\Delta(u-r) - \Delta(g-i) < 0$ displays dust-reddened curvature, while an object with $\Delta(u-r) - \Delta(g-i) > 0$ displays a red power-law. We use this criterion to classify quasars as intrinsically red, as shown in Figure 6 (discussed in §4.2).

Since relative colors compare the observed quasar colors to the mean colors for quasars at that redshift, atypical emission lines will affect the relative color results. For the redshift range $1 < z < 2$, the most significant lines are MgII and the FeII emission line blend. To correct for atypical MgII lines, we calculate the equivalent width of MgII from the spectrum. From this, we subtract the average MgII equivalent width obtained from the Vanden Berk composite spectrum (2001). The residual MgII line flux is calculated and added or subtracted from the band where MgII is found. To correct for the FeII emission line blend, we redden the composite spectrum, shift it to the observed frame, and normalize to the source spectrum. We then subtract this spectrum from the source for the range 2200-2700 Å and calculate the equivalent width of the residual FeII line. We add or subtract the residual flux from the bands where FeII is found. Since the u band is outside of the spectral range, we cannot correct for atypical emission lines in this band. The relative colors and the optical continuum shapes are listed in Table 5.

3.3. X-ray Spectral Fits

We made fits to the extracted spectra using the *Sherpa* package⁸ within CIAO⁹. For each source, the available MOS+PN spectra were fit simultaneously by linking parameters. We used a conservative spectral range of 0.5 - 10 keV for fitting. The observations were fit according to their S/N, with more complicated models (models A-E) being applied as S/N increased. Table 6 summarizes the

⁸ <http://cxc.harvard.edu/sherpa/threads/index.html>

⁹ <http://cxc.harvard.edu/ciao/>

TABLE 5
RELATIVE COLORS AND THE OPTICAL CONTINUUM SHAPE

ID	$\Delta(u-r)$	$\Delta(g-i)$	$\Delta(r-z)$	Continuum Shape
1	0.97 \pm 0.06	0.68 \pm 0.06	0.13 \pm 0.04	Dust
2	0.96 \pm 0.07	0.25 \pm 0.04	0.03 \pm 0.07	Dust
3	0.79 \pm 0.04	0.41 \pm 0.03	0.29 \pm 0.04	Dust
4	1.26 \pm 0.08	0.81 \pm 0.03	0.65 \pm 0.04	Dust
5	0.63 \pm 0.04	0.71 \pm 0.04	0.16 \pm 0.04	Red power-law ($\alpha_{opt} = -1.36$)
6	1.06 \pm 0.07	0.83 \pm 0.03	0.52 \pm 0.05	Dust
7	1.10 \pm 0.06	0.69 \pm 0.02	0.23 \pm 0.04	Dust
8	1.13 \pm 0.06	0.74 \pm 0.04	0.58 \pm 0.04	Dust
9	0.99 \pm 0.07	0.77 \pm 0.03	0.56 \pm 0.04	Dust
10	0.77 \pm 0.07	0.74 \pm 0.03	0.41 \pm 0.06	Undefined
11	0.80 \pm 0.07	0.74 \pm 0.05	0.47 \pm 0.04	Undefined
12	0.14 \pm 0.04	0.24 \pm 0.03	0.06 \pm 0.04	Red power-law ($\alpha_{opt} = -0.87$)
13	-0.07 \pm 0.07	0.54 \pm 0.05	0.56 \pm 0.1	Red power-law ($\alpha_{opt} = -1.44$)
14	0.60 \pm 0.07	0.54 \pm 0.03	0.38 \pm 0.08	Undefined
15	0.54 \pm 0.08	0.63 \pm 0.04	0.40 \pm 0.09	Red power-law ($\alpha_{opt} = -1.94$)
16	0.33 \pm 0.04	0.44 \pm 0.03	0.26 \pm 0.04	Red power-law ($\alpha_{opt} = -1.17$)
17	0.25 \pm 0.02	0.40 \pm 0.02	0.20 \pm 0.03	Red power-law ($\alpha_{opt} = -1.31$)

NOTE. — The relation between the relative colors gives the optical continuum shape from the photometry. $\Delta(u-r) > \Delta(g-i) > \Delta(r-z)$ indicates dust, but $\Delta(u-r) < \Delta(g-i) > \Delta(r-z)$ indicates a red power-law.

model characteristics. All models applied in this paper include local absorption fixed to the Galactic hydrogen column density ($N_{H,gal}$) for a source’s coordinates. Values for $N_{H,gal}$ were taken from WebPIMMS¹⁰.

For six observations with $S/N < 4$, we fit Model A, where we freeze the photon index of the X-ray power-law to $\Gamma = 1.9$. We leave normalization free to vary in order to get the flux or a 90% upper-limit on the flux. For five observations with $2 < S/N < 4$, we fit Model B, a single power-law with free Γ and normalization. Models A and B use the Cash statistic for fitting, which we discuss further below.

For 14 observations with $S/N > 4$, we fit Model C, a single power-law, but using Chi-square statistics rather than Cash. For the same observations, we also fit the spectra with Model D, a power-law with intrinsic absorption. Finally, for five observations with $S/N > 25$, we fit model E, a power-law with intrinsic absorption, plus a Gaussian for the Fe $K\alpha$ line. The Gaussian line energy is set to 6.4 keV shifted to the quasar’s reference frame. For sources with $S/N > 4$ (where models C, D and E are applied), the Chi-square statistic is used and the data are binned by at least 15 counts/bin.

For $S/N < 4$, Chi-square is not an appropriate statistic because there are not enough counts per bin, so both models A and B are fit using the more time-consuming Cash statistic (1979) which gives more reliable results for low-count sources (Nousek & Shue 1989). When using Cash statistics, the source and background counts are binned by one count/bin, to ensure that there are no empty bins. The background is not subtracted and is instead fit simultaneously with the source. The XMM background is fit with the three components described in the XMM Users Handbook¹¹: a power-law fixed to $\Gamma = 1.4$ plus Galactic absorption (to account for the extragalactic X-ray spectrum), a broken power-law, with the break energy fixed to 3.2 keV (to account for the quiescent soft proton spectrum), and lines at 1.5 keV for the MOS cameras and at 1.5 and 8 keV for the PN camera (to account for cosmic-ray interactions with the

detector). Since this background model has five free parameters for each camera, constraining all fit parameters results in large errors in the best-fit parameters.

Table 7 lists the source ID, the model used for each source, XMM observation ID, the best-fit spectral slopes, flux values from 0.5-2 keV and 2-10 keV, the rest-frame 2-10 keV luminosity, and the χ^2 or Likelihood of Fit values and degrees of freedom for the best fit. For sources with $S/N < 4$, Table 7 lists the best-fit parameters for Model A, where the spectral slope is fixed to 1.9, leaving the normalization free to vary. (For sources with $S/N < 2$, the best-fit upper-limits are listed.) We list the best-fit spectral slopes from Model B in Table 8 for reference, but due to the large spectral slope errors we do not use these values for further analysis.

For sources with $S/N > 4$, we determine the best-fit model via the F-test¹², which measures the significance of the change in chi-square as components are added to a model. In all cases, the more complex models did not have a significantly lower chi-square value, so for $S/N > 4$, Table 7 lists the parameters for the power-law model (model C).

Tables 8 and 9 list the best-fit spectral slope and the upper-limits on other spectral parameters for rejected models B and D (Table 8) and E (Table 9). Figure 3 shows the data, fits, residuals and 1σ , 2σ and 3σ Γ - N_H contours for the sources with $S/N > 4$ fitted with model D (power-law + intrinsic absorption).

3.4. X-ray Absorption

Of the 11 sources (and 14 observations) with $S/N > 4$, none show significant intrinsic absorption, and the F-test demonstrates that all sources prefer a simple power-law model. N_H upper limits (Model D) for the five highest S/N sources range from $3 \times 10^{20} \text{ cm}^{-2}$ to $2 \times 10^{21} \text{ cm}^{-2}$ at the 90% confidence level.

Absorption can also be indicated when the best-fitting power-law is unusually hard. Mateos et al. (2005) finds an average X-ray photon index $\langle \Gamma \rangle \sim 1.96$ and intrinsic dispersion $\sigma_\Gamma = 0.4$ for a sample of 1137 AGN found in XMM-Newton fields, with fluxes ranging from

¹⁰ <http://heasarc.gsfc.nasa.gov/Tools/w3pimms.html>

¹¹ http://xmm.vilspa.esa.es/external/xmm_user_support/documentation

¹² <http://cxc.harvard.edu/ciao/ahelp/ftest.html>

TABLE 6
S/N-DEPENDENT MODELS APPLIED TO XMM OBSERVATIONS

	Model A	Model B	Model C	Model D	Model E
S/N	S/N < 4	2 < S/N < 4	S/N > 4	S/N > 4	S/N > 25
Model	Cash fit	Cash fit	χ^2 fit	χ^2 fit	χ^2 fit
Description	Fixed power-law ($\Gamma = 1.9$) Gal. abs. (fixed)	Free power-law Gal. abs. (fixed)	Free power-law Gal. abs. (fixed)	Free power-law Gal. abs. (fixed) Intrinsic abs. (free)	Free power-law Gal. abs. (fixed) Intrinsic abs. (free) Fe K α line

NOTE. — A total of 22 observations cover 17 sources.

TABLE 7
BEST-FIT X-RAY SPECTRAL FITS

Source ID	Model	XMM ID	Γ	$F_{0.5-2keV}^a$	$F_{2-10keV}^a$	$L_{2-10keV}^b$	χ^2/ν^c
1	A	0201290301	1.9 ^d	<0.024	<0.034	$<9.5 \times 10^{41}$	1791/1599
2	A	0200730401	1.9	0.24	0.36	5.2×10^{42}	8904/5766
3a	A	0113060401	1.9	<0.51	<3.72	$<3.6 \times 10^{43}$	1225/1603
3b	A	0113060201	1.9	2.25	3.10	4.8×10^{43}	1018/1614
4	A	0145450501	1.9	0.016	13.4	5.2×10^{43}	1608/1619
5a	A	0203360401	1.9	0.32	0.46	1.3×10^{43}	17119/5749
5b	A	0203360801	1.9	0.53	0.74	2.1×10^{43}	10447/4946
6	A	0009650201	1.9	0.52	2.96	3.2×10^{43}	1831/1636
7	C	0039140101	1.8 ^{+0.5} _{-0.4}	1.95	3.05	7.7×10^{43}	4.3/6
8	C	0110990201	1.0 ^{+0.4} _{-0.4}	1.36	7.49	7.0×10^{43}	9.7/7
9a	C	0110930401	1.4 ^{+0.4} _{-0.4}	2.78	7.96	1.3×10^{44}	2.6/5
9b	C	0110930901	1.0 ^{+0.4} _{-0.4}	4.57	27.2	2.7×10^{44}	3.7/7
10	C	0009650201	1.9 ^{+0.4} _{-0.3}	3.05	4.90	9.4×10^{43}	2.6/6
11	C	0143650901	1.5 ^{+0.3} _{-0.3}	5.03	13.3	1.5×10^{44}	5.9/9
12	C	0149900201	1.4 ^{+0.5} _{-0.4}	8.58	16.2	3.0×10^{44}	8.1/15
13	C	0081340201	1.6 ^{+0.1} _{-0.1}	9.59	20.7	2.8×10^{44}	27/40
14	C	0203361801	1.75 ^{+0.09} _{-0.09}	6.52	11.9	1.6×10^{44}	54/63
15	C	0203361801	1.78 ^{+0.07} _{-0.06}	17.0	29.5	3.4×10^{44}	75/107
16a	C	0147511701	1.77 ^{+0.06} _{-0.05}	12.1	20.1	2.9×10^{44}	100/165
16b	C	0147511801	1.72 ^{+0.06} _{-0.05}	13.2	23.5	3.2×10^{44}	155/189
17a	C	0143150301	1.68 ^{+0.05} _{-0.06}	60.6	120	1.8×10^{45}	94/142
17b	C	0143150601	1.72 ^{+0.04} _{-0.03}	57.9	107	1.7×10^{45}	203/311

^aFluxes are determined from the MOS-1 observations because it has the best (most well-known) calibration. Units are 10^{-14} ergs $\text{cm}^{-2} \text{s}^{-1}$.

^bLuminosities are in rest-frame in units of ergs s^{-1} .

^cThis column contains either the chi-square value and the degrees of freedom when chi-square statistics are applied (model C) or the likelihood of fit and the degrees of freedom when the Cash statistic is applied (model A).

^d Γ is fixed to 1.9 for model A.

10^{-15} - 10^{-12} ergs $\text{cm}^{-2} \text{s}^{-1}$. Mateos et al. (2005) find a systematic hardening of the average X-ray spectra towards fainter fluxes, which they interpret as a higher degree of photoelectric absorption among fainter AGNs. Therefore, we define an unusually hard spectrum to have $\Gamma < 1.5$ at 90% confidence. Two of 14 sources with S/N > 4 have unusually hard spectral slopes by this measure: SDSS J1226+0130 (#8) and SDSS J1435+4841 (#9). All of the quasars with high enough S/N to fit Γ have best-fit spectral slopes flatter than the Mateos et al. (2005) average.

For the five sources with $2 < \text{S/N} < 4$ (fit with model A), the S/N is not high enough to fit a power-law or intrinsic absorption. One indicator of X-ray absorption

for these sources is X-ray weakness relative to the optical luminosity, defined as $\alpha_{ox} < -1.8$, where α_{ox} is the spectral index from 2500 Å to 2 keV. Such small values of α_{ox} are a common characteristic of BAL quasars, which are known to be heavily absorbed objects in the X-rays (Mathur et al. 1995; Green & Mathur 1996).

To calculate α_{ox} for the red sample, we use the 2 keV flux (F_{2keV}) given by the X-ray fits, and we derive the 2500 Å flux (F_{uv}) by interpolating a power-law between the nearest two of the *ugriz* magnitudes. We then calculate $\alpha_{ox,corr}$ by correcting α_{ox} for absorption. We deredden F_{uv} using $E(B-V)_{spec}$ and the Prevot et al. (1984) SMC extinction curve, where $A_\lambda = E(B-V) 1.39 \lambda^{-1.2}$. For objects with X-ray S/N > 4, we do not find signifi-

TABLE 8
ALTERNATIVE X-RAY SPECTRAL FITS: Γ ($S/N < 4$) AND $N_{H,x}$ ($S/N > 4$)

Model	Source ID	XMM ID	Γ	$N_{H,x}$ (10^{22} cm^{-2})	χ^2/ν^a
B	2	0200730401	$1.8^{+8.6}_{-4.0}$	-	8949/5767
B	3a	0113060401	$1.2^{+2.1}_{-2.3}$	-	1015/1614
B	4	0145450501	$1.2^{+2.3}_{-2.8}$	-	1418/1619
B	5a	0203360401	$2.0^{+16.2}_{-3.9}$	-	17008/5750
B	5b	0203360801	$2.5^{+18.5}_{-4.9}$	-	11003/4946
B	6	0009650201	$1.2^{+2.7}_{-2.9}$	-	1822/1636
D	7	0039140101	$1.8^{+0.5}_{-0.4}$	≤ 7.0	3.5/5
D	8	0110990201	$1.0^{+0.4}_{-0.4}$	≤ 13.4	8.0/5
D	9a	0110930401	$1.4^{+0.4}_{-0.4}$	≤ 6.8	2.6/4
D	9b	0110930901	$1.0^{+0.4}_{-0.4}$	≤ 10.2	3.6/6
D	10	0009650201	$1.9^{+0.4}_{-0.3}$	≤ 3.3	2.2/5
D	11	0143650901	$1.5^{+0.3}_{-0.3}$	≤ 0.9	5.9/8
D	12	0149900201	$1.4^{+0.3}_{-0.4}$	≤ 0.8	7.3/14
D	13	0081340201	$1.6^{+0.1}_{-0.1}$	≤ 0.2	27/39
D	14	0203361801	$1.75^{+0.09}_{-0.09}$	≤ 0.05	54/62
D	15	0203361801	$1.78^{+0.07}_{-0.06}$	≤ 0.05	75/106
D	16a	0147511701	$1.77^{+0.06}_{-0.05}$	≤ 0.06	100/164
D	16b	0147511801	$1.72^{+0.06}_{-0.05}$	≤ 0.04	155/188
D	17a	0143150301	$1.68^{+0.05}_{-0.06}$	≤ 0.04	94/141
D	17b	0143150601	$1.72^{+0.04}_{-0.03}$	≤ 0.02	203/310

NOTE. — For sources with $S/N < 4$, model parameters from the Model B (Cash power-law) fits are given. For sources with $S/N > 4$, we list 90% confidence upper-limits on Model D, power-law + intrinsic absorption.

^aThis column contains either the chi-square value and the degrees of freedom when chi-square statistics are applied (model C) or the likelihood of fit and the degrees of freedom when the Cash statistic is applied (model A).

TABLE 9
ALTERNATIVE X-RAY SPECTRAL FITS - Fe K α LINE ($S/N > 25$)

Source ID	Model	XMM ID	Fe K α FWHM ^a (eV)	Fe K α line flux ^a (photons $\text{cm}^{-2} \text{ s}^{-1}$)	χ^2/ν^b
15	E	0203361801	≤ 10	$\leq 2.6\text{e-}6$	72.3/102
16a	E	0147511701	≤ 220	$\leq 3.6\text{e-}7$	100.2/160
16b	E	0147511801	≤ 440	$\leq 2.5\text{e-}6$	145.8/184
17a	E	0143150301	≤ 190	$\leq 3.8\text{e-}4$	92.2/137
17b	E	0143150601	≤ 0	$\leq 3.3\text{e-}6$	194.5/306

^aFe K α line parameter upper-limits are given at 90% confidence.

^bThe χ^2 value and the degrees of freedom (ν) for χ^2 statistics.

cant intrinsic absorption, so we use the 90% upper-limit on N_H to correct F_{2keV} . For objects with X-ray $S/N < 4$, we cannot fit intrinsic absorption, so we make no correction to F_{2keV} . Table 10 gives the measured and corrected F_{uv} and F_{2keV} , α_{ox} (uncorrected), and $\alpha_{ox,corr}$ (corrected for absorption).

Figure 4 plots α_{ox} against the log of the 2500 Å luminosity (l_{uv}) for the red sample. The unfilled circles give the measured α_{ox} and l_{uv} values for the red sample. The filled circles give $\alpha_{ox,corr}$ and $l_{uv,corr}$, the 2500 Å luminosity corrected for absorption. Solid lines connect the uncorrected values to the corrected values for each source. The five sources with X-ray $S/N < 4$ are marked in red. The Strateva et al. (2005) sample and $\alpha_{ox} - l_{uv}$ correlation are plotted as black points and a solid line, respectively, for comparison. The dotted line marks $\alpha_{ox} = -1.8$; those sources with $\alpha_{ox} < -1.8$ are X-ray weak relative to the optical luminosity. All five sources with 2

$< S/N < 4$ are X-ray weak, possibly because we were unable to correct the X-ray flux for absorption. All eleven sources with $S/N > 4$ are X-ray normal once corrected for absorption ($\alpha_{ox,corr} > -1.8$).

Correction for absorption can have a large effect on F_{2keV} , which can in turn have a large effect on α_{ox} . The largest correction in our sample, for an N_H upper-limit of 10^{23} cm^{-2} , led to a factor of 9.5 change in F_{2keV} . An additional correction for dust-reddening changed F_{uv} by a factor of 3, leading to $\Delta(\alpha_{ox}) = 0.2$. Sources with low S/N and/or high N_H upper-limits will have a large but undetermined uncertainty in α_{ox} , which makes it difficult to tell if the source is intrinsically weak relative to the optical, or if the X-ray weakness is due only to absorption.

There is a weak correlation between α_{ox} and Γ (Spearman Rank = 0.13) such that X-ray weak objects are slightly more likely to have flatter spectral slopes.

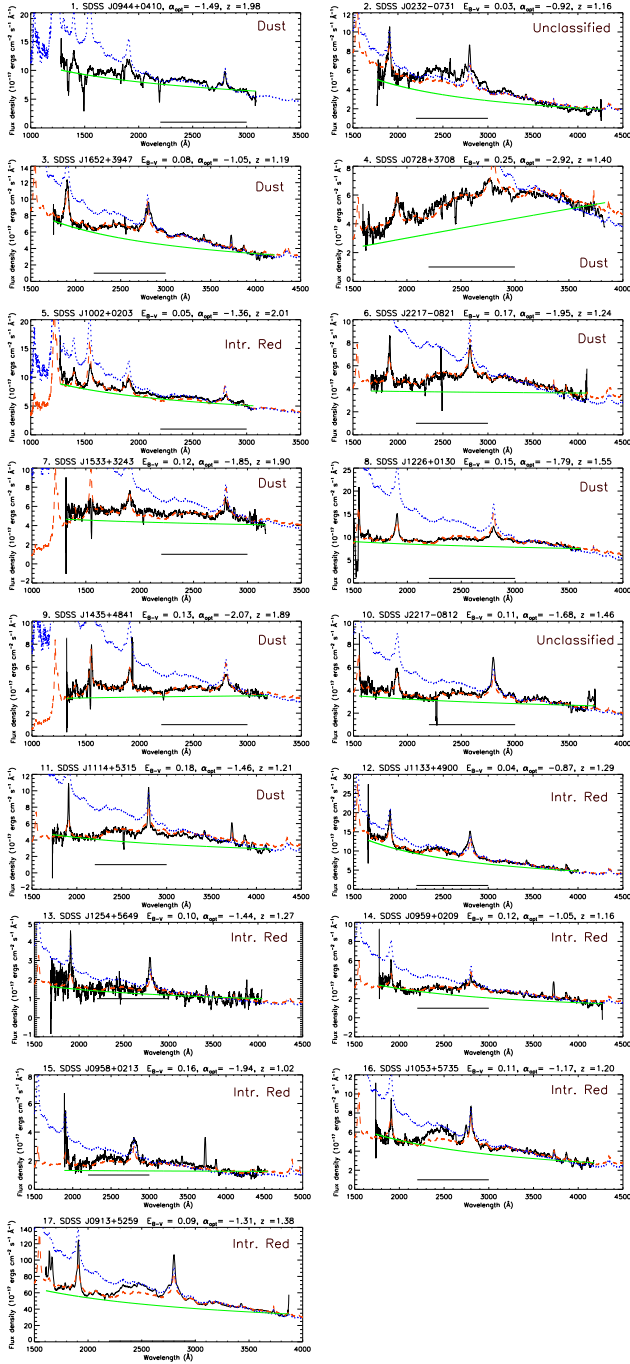


FIG. 2.— The SDSS source spectra are plotted as solid black lines, F_λ (10^{-17} ergs $\text{cm}^{-2} \text{s}^{-1} \text{\AA}^{-1}$) vs. λ (\AA). The original Vanden Berk et al. (2001) template (dotted, blue line) and the reddened template (dashed, red line) are overplotted. Note that the BAL quasar (SDSS J0944+0410, #1) had no reliable continuum to fit reddening and so only the original template is plotted. The solid line beneath the spectrum marks the FeII+MgII region ignored by the continuum-fitting program as described in the text. A power-law fit to the spectrum, omitting major emission lines, is also shown (solid, green line).

4. DISCUSSION

The redshift selection minimizes the chance that host galaxy emission or Ly α forest absorption produce the observed red colors of these quasars. This leaves two possible causes of red colors: dust-reddening or intrinsically red optical continua. Table 11 summarizes the source

TABLE 10
X-RAY STRENGTH RELATIVE TO THE OPTICAL

ID	F_{uv}^a	$F_{uv,corr}^b$	F_{2keV}^c	$F_{2keV,corr}^d$	α_{ox}	$\alpha_{ox,corr}^e$
1	3.87	6.04	<2.45	<2.45	<-1.61	<-1.69
2	3.19	3.99	0.33	0.33	-1.91	-1.95
3a	4.39	7.54	<0.17	<0.17	<-2.07	<-2.16
3b	4.39	7.54	3.08	3.08	-1.59	-1.68
4	2.85	15.05	2.81	2.81	-1.54	-1.82
5a	2.69	3.83	0.38	0.38	-1.86	-1.92
5b	2.69	3.83	0.67	0.67	-1.77	-1.83
6	5.00	15.66	0.15	0.15	-2.12	-2.31
7	2.53	5.82	2.75	29.0	-1.52	-1.27
8	5.65	15.34	0.77	7.24	-1.87	-1.66
9a	2.10	5.06	1.87	45.1	-1.55	-1.17
9b	2.10	5.06	1.38	3.67	-1.61	-1.59
10	2.64	5.67	4.32	10.0	-1.45	-1.44
11	5.34	17.66	4.57	8.44	-1.56	-1.66
12	7.39	9.88	7.36	10.6	-1.54	-1.52
13	1.33	2.64	9.72	10.9	-1.20	-1.30
14	2.20	5.09	7.79	8.02	-1.32	-1.46
15	2.21	6.47	21.9	22.6	-1.15	-1.33
16a	4.42	9.48	14.7	15.1	-1.33	-1.45
16b	4.42	9.48	15.2	15.6	-1.33	-1.45
17a	53.67	95.96	63.5	64.5	-1.51	-1.60
17b	53.67	95.96	63.8	64.4	-1.51	-1.60

^aRest-frame 2500 \AA fluxes are in units of 10^{-28} ergs $\text{cm}^{-2} \text{s}^{-1} \text{Hz}^{-1}$.

^bThe 2500 \AA flux is corrected using $E(B-V)_{spec}$.

^cRest-frame 2 keV fluxes are in units of 10^{-32} ergs $\text{cm}^{-2} \text{s}^{-1} \text{Hz}^{-1}$.

^dFor sources with S/N > 4, the 2 keV flux is corrected for the N_H 90% confidence upper-limit. (No 2 keV flux correction is made for sources with IDs #1-7.)

^e $\alpha_{ox,corr}$ is calculated with $F_{uv,corr}$ and $F_{2keV,corr}$ so that it is corrected for dust-reddening and, where possible, an upper-limit on X-ray absorption.

characteristics of the SDSS/XMM red quasar sample, which guide the classification of a source as ‘absorbed’ or ‘intrinsically red.’ We discuss dust-reddened quasars in §4.1 and intrinsically red quasars in §4.2. §4.3 discusses two quasars that we were not able to classify. We comment on the general properties of the red sample in terms of the α_{ox} - l_{uv} relation (§4.5) and the X-ray spectral slope (§4.4). Finally, we discuss properties of the intrinsically red quasars in (§4.5).

4.1. Dust-reddened Quasars with X-ray Absorption

By the criteria shown in Table 11, 8 of 17 quasars in the sample are dust-reddened. $E(B-V)_{spec}$ is significant at $\geq 3\sigma$ for all eight sources. Seven of 8 sources have optical continuum shapes consistent with dust-reddened curvature. (The exception, SDSS J1114+5315 (#11), has larger errors on the relative colors, resulting in an ambiguous continuum shape. However, strong $E(B-V)_{spec}$ and X-ray weakness argue in favor of dust-reddening.)

SDSS J0944+0410 (#1) is a low-ionization BAL quasar (Voit et al. 1993), with Si IV, C IV, C III, C II] and Mg II absorption troughs of widths $\sim 2,000$ - $5,000 \text{ km s}^{-1}$ (Fig. 2). BALs are known to be heavily absorbed in the optical and the X-rays (Green et al. 2001). This source is undetected in the X-rays (upper-limit in Fig. 4). Due to the numerous absorption lines and a strong FeII bump, we were not able to fit a reddening to the spectral continuum, so the flatness of the spectrum could be due either to line absorption, continuum absorption, or an intrinsically different continuum. However, some research suggests that BALs tend to have redder continua than

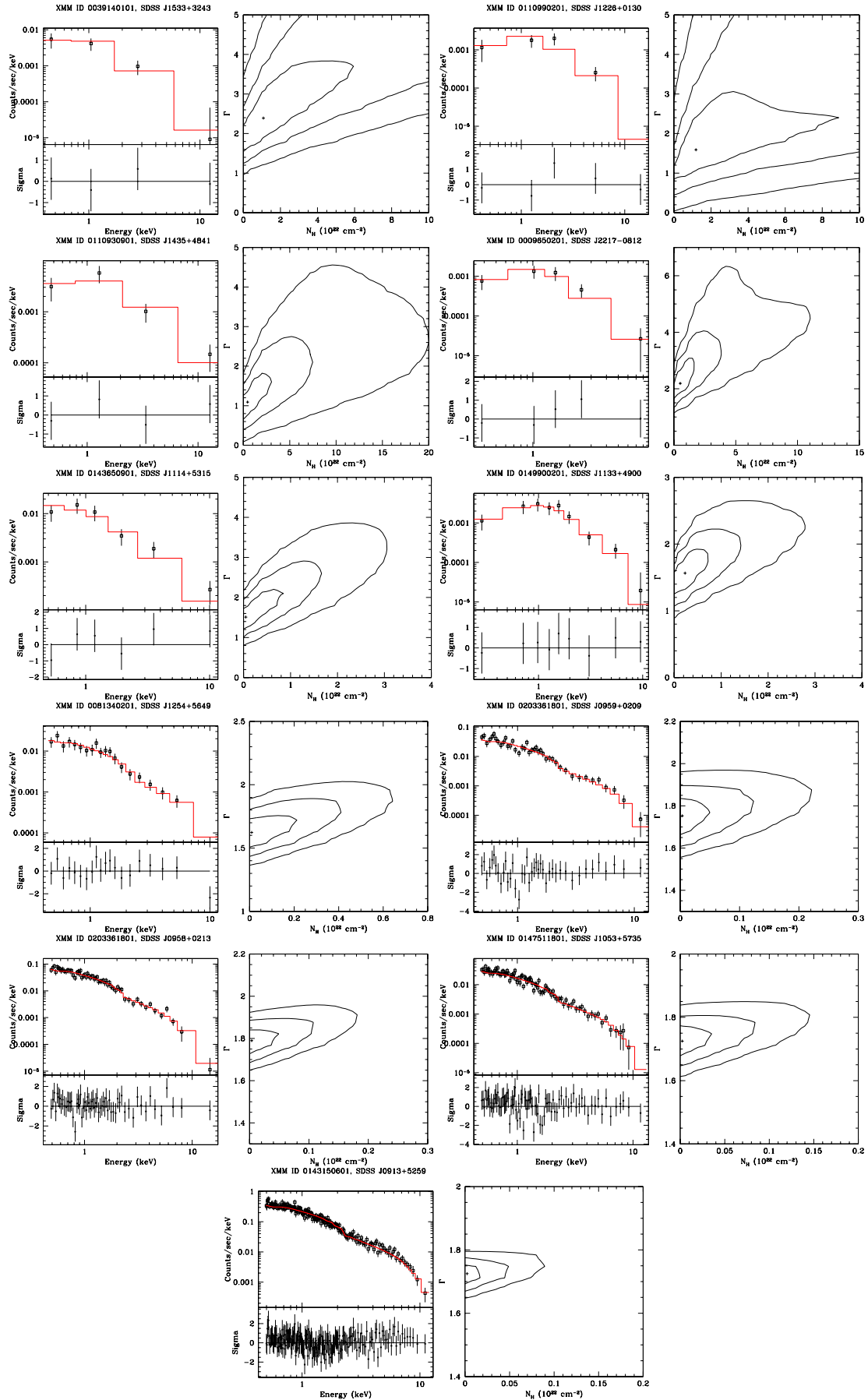


FIG. 3.— For each pair of figures, the left column plots the data for sources with $S/N > 4$ on a log scale, photons $s^{-1} \text{keV}^{-1}$ versus energy (keV). The data are fit with model D (power-law + intrinsic absorption, data binned to 15 counts per bin). The model, which has been folded through the detector response, is plotted as a histogram over the data. Residuals are plotted underneath the fits in units of standard deviation. The right column contains Γ - N_H contour plots, where the 1 σ , 2 σ and 3 σ contours are plotted as solid lines. The plots correspond to sources #7-#17, starting with #7 in the top left panel. Each pair of plots is labeled with the SDSS name and XMM observation ID.

TABLE 11
SUMMARY OF SOURCE CHARACTERISTICS

ID	SDSS name	Γ	$\alpha_{ox,corr}$ ^a	$N_{H,x}$	$E(B-V)_{spec}$ 10^{22} cm^{-2}	$N_{H,x}/$ $E(B-V)_{spec}$ ^b	Optical Continuum ^c	Notes
Absorbed Quasars								
1	SDSS J0944+0410	1.9	<-1.69	-	-	-	Dust	BAL
3	SDSS J1652+3947	1.9	-1.92	-	0.08 ± 0.02	-	Dust	
4	SDSS J0728+3708	1.9	-1.82	-	0.25 ± 0.02	-	Dust	
6	SDSS J2217-0821	1.9	-2.31	-	0.17 ± 0.02	-	Dust	
7	SDSS J1533+3243	$1.8^{+0.5}_{-0.4}$	-1.27	≤ 7.0	0.12 ± 0.01	≤ 100	Dust	
8	SDSS J1226+0130	$1.0^{+0.4}_{-0.4}$	-1.66	≤ 13.4	0.15 ± 0.01	≤ 143	Dust	NAL
9	SDSS J1435+4841	$1.2^{+0.3}_{-0.3}$	-1.38	≤ 6.8	0.13 ± 0.01	≤ 100	Dust	NAL
11	SDSS J1114+5315	$1.5^{+0.3}_{-0.3}$	-1.66	≤ 0.9	0.18 ± 0.03	≤ 8	Undefined	
Intrinsically Red Quasars								
5	SDSS J1002+0203	1.9	-1.87	-	0.052 ± 0.005	-	Red power-law	
12	SDSS J1133+4900	$1.4^{+0.5}_{-0.4}$	-1.52	≤ 0.8	0.04 ± 0.01	≤ 20	Red power-law	
13	SDSS J1254+5649	$1.6^{+0.1}_{-0.1}$	-1.30	≤ 0.2	$0.10^{+0.11}_{-0.08}$	≤ 3	Red power-law	
14	SDSS J0959+0209	$1.75^{+0.09}_{-0.09}$	-1.46	≤ 0.05	0.12 ± 0.03	≤ 0.6	Undefined	
15	SDSS J0958+0213	$1.78^{+0.07}_{-0.06}$	-1.33	≤ 0.05	$0.16^{+0.09}_{-0.07}$	≤ 0.5	Red power-law	
16	SDSS J1053+5735	$1.75^{+0.04}_{-0.04}$	-1.45	≤ 0.06	0.11 ± 0.02	≤ 0.9	Red power-law	
17	SDSS J0913+5259	$1.70^{+0.03}_{-0.03}$	-1.60	≤ 0.03	$0.086^{+0.004}_{-0.003}$	≤ 0.6	Red power-law	
Unclassified Quasars								
2	SDSS J0232-0731	1.9	-1.95	-	0.03 ± 0.02	-	Dust	
10	SDSS J2217-0812	$1.9^{+0.4}_{-0.3}$	-1.44	≤ 1.8	$0.11^{+0.03}_{-0.02}$	≤ 20	Undefined	

NOTE. — For absorbed quasars, a value is bold-faced if the source matches one of the criteria for dust-reddening in the optical/UV or absorption in the X-rays. Criteria for dust-reddening are: a) strong spectroscopic reddening ($E(B-V)_{spec} > 0.1$) detected to $> 3\sigma$ confidence and b) an optical continuum shape that indicates dust-reddening. The criteria for X-ray absorption are: a) weak X-ray flux relative to the optical ($\alpha_{ox} < -1.8$), b) a flat X-ray spectral slope ($\Gamma < 1.5$ to greater than 90% confidence), and c) a large gas column upper-limit (N_H upper-limit $> 10^{22} \text{ cm}^{-2}$ if intrinsic absorption fits are applied. For intrinsically red quasars, a value is bold-faced if the source matches one of the criteria of an intrinsically red power-law: a) reddening is mild ($E(B-V)_{spec} < 0.1$) or detected at $< 3\sigma$, b) an optical continuum shape that contra-indicates dust-reddening, c) a low X-ray gas column upper-limit (N_H upper-limits $< 10^{22} \text{ cm}^{-2}$), and d) gas/dust ratio smaller than the Galactic value.

^a $\alpha_{ox,corr}$ is calculated with $F_{uv,corr}$ and $F_{2keV,corr}$ so that it is corrected for dust-reddening and, where possible, for X-ray absorption upper-limits.

^bThe measured gas/dust ratio relative to the Galactic value, $5.8 \times 10^{21} \text{ cm}^{-2}$ (Bohlin et al. 1978; Kent et al. 1991).

^cThe optical continuum shape is defined by the relationship between the relative colors (§3.4, Table 5).

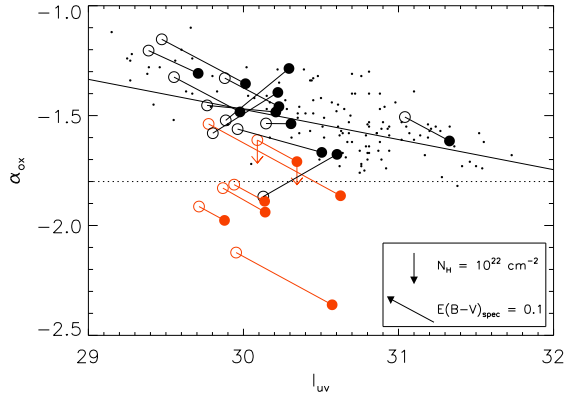


FIG. 4.— α_{ox} vs. l_{uv} for the red quasar sample, where l_{uv} is the log of the 2500 Å luminosity in units of $\text{ergs cm}^{-2} \text{s}^{-1} \text{Hz}^{-1}$. The unfilled circles give the measured l_{uv} and α_{ox} values for the red quasar sample. The filled circles give $l_{uv,corr}$ and $\alpha_{ox,corr}$, where the 2500 Å flux has been corrected for $E(B-V)_{spec}$ and the 2 keV flux has been corrected for the upper-limit on N_H . The six sources with X-ray S/N < 4 are corrected for $E(B-V)_{spec}$ only and not N_H ; these sources are marked in red. The S06 $\alpha_{ox} - l_{uv}$ correlation is plotted as a solid line and the S05 sample is overlaid in black points. The dotted line marks $\alpha_{ox} = -1.8$. Sources with $\alpha_{ox} < -1.8$ are defined to be X-ray weak. The legend shows the correction to α_{ox} and l_{uv} for an $E(B-V)_{spec} = 0.1$ and the correction to α_{ox} for an N_H upper-limit of 10^{22} cm^{-2} . Both of the corrections shown in the legend were calculated for the samples median redshift, $z=1.3$.

non-BALs, and dust-reddened templates appear to be a good fit to BAL continua (Yamamoto & Vanzsevicius 1999; Brotherton et al. 2001; Tolea et al. 2002; Reichard et al. 2003). We therefore conclude that this quasar is likely to have dust-reddening and X-ray absorption.

All 8 sources match some of the criteria for X-ray absorption. For the three sources with $2 < S/N < 4$ (where X-rays are detected but no X-ray spectral fits can be made), all are X-ray weak when the optical luminosity is corrected for dust-reddening ($\alpha_{ox,corr} < -1.8$). These sources are discussed further in §4.4.

Four of the 8 dust-reddened quasars have X-ray S/N > 4, which allows us to fit a power-law (model C) and a power-law plus intrinsic absorption (model D). All four sources prefer model C over model D, but two quasars have abnormally flat ($\Gamma < 1.5$) photon indices to 90% confidence: SDSS J1226+0130 (#8) and SDSS J1435+4841 (#9). This may be a sign of large N_H columns. In addition, the upper-limits on N_H for all four sources are rather high ($9 \times 10^{21} - 1 \times 10^{23} \text{ cm}^{-2}$, Table 8), and are consistent with the gas column predicted from $E(B-V)_{spec}$ ($N_{H,opt} = 7.0 \times 10^{20} - 1 \times 10^{21} \text{ cm}^{-2}$) using the Galactic gas-to-dust ratio (Bohlin et al. 1978; Kent et al. 1991). Even the ten times higher N_H expected from an SMC gas-to-dust ratio (Issa et al. 1990), which is more typical for quasars (Maccacaro & Perola 1981; Maiolino et al. 2001; Wilkes et al. 2002), is still below the N_H upper-limit found in the X-rays.

Note that the quasars classified as dust-reddened occupy the lower half of the red quasar sample with respect to S/N. The low S/N for these quasars is likely due to the photoelectric absorption of the X-rays, as described above. The effect of N_H on the X-ray spectrum is further discussed in §4.5.

4.2. Intrinsically Red Quasars

Seven sources display mild or insignificant dust-reddening: $E(B-V)_{spec} \leq 0.1$ or $E(B-V)_{spec}$ detected at $< 3\sigma$. Since the reddening in these sources is indistinguishable from a red power-law (§3.2), we classify them as intrinsically red using two additional indicators: (1) the continuum shape as determined by the relative photometry (§3.2) and (2) the lack of X-ray absorption (§3.4).

The optical continuum shape is inconsistent with dust-reddening for all but one object. The relative colors for SDSS J0959+0209 (#14) cannot distinguish between dust curvature and a red power-law; however, this source meets all of the other ‘intrinsically red’ criteria. Six of seven sources also display no significant X-ray absorption, with low N_H upper-limits of $\sim 10^{20} - 10^{21} \text{ cm}^{-2}$. These same six sources are X-ray normal ($\alpha_{ox,corr} > -1.8$), and are not abnormally X-ray flat ($\Gamma > 1.5$ to 90% confidence). It is not surprising then that these six sources have the highest X-ray S/N of the red quasar sample, due to the absence of X-ray absorption. The exception is SDSS J1002+0203 (#5), whose low S/N (S/N = 2.85) prohibits fitting a power-law or intrinsic absorption. This source is X-ray weak ($\alpha_{ox} = -1.82$), but the low amount of dust-reddening ($E(B-V)_{spec} = 0.052 \pm 0.005$) suggests that the X-ray weakness is intrinsic. If we assume an SMC gas/dust ratio, then a reddening of 0.05 leads to an X-ray absorption column of $N_H = 3 \times 10^{21} \text{ cm}^{-2}$. However, a column of less than 10^{22} cm^{-2} will not significantly affect the rest-frame 2 keV flux (Tucker 1975).

For the four sources with the highest X-ray S/N, SDSS J0959+0209 (#14), SDSS J0958+0213 (#15), SDSS J1053+5735 (#16) and SDSS J0913+5259 (#17), the low N_H upper-limits imply gas-to-dust ratio upper-limits (Table 8) up to a factor of ~ 2 smaller than the Galactic value (Bohlin et al. 1978; Kent et al. 1991) and a factor of ~ 20 below the SMC value (Issa et al. 1990) (Figure 5). The small dust-to-gas ratio found for these four objects contrasts with previous studies, which have shown that an SMC-type extinction curve and high gas-to-dust ratio is most appropriate for quasar absorption (Maccacaro & Perola 1981; Maiolino et al. 2001; Wilkes et al. 2002). For example, Maiolino et al. (2001) collected X-ray and optical information for 19 objects from the literature. They find gas-to-dust ratios 3-100 times higher than Galactic for sixteen AGNs. The three AGNs with gas-to-dust ratios a factor ~ 1.5 below the Galactic value were all low luminosity AGNs ($L_x < 10^{42} \text{ ergs s}^{-1}$). For comparison, all of the red quasars have $L_x > 10^{42} \text{ ergs s}^{-1}$, with the exception of the BAL quasar (#1). The smaller filled circles in Fig. 5 mark points from Maiolino et al. (2001). Median error bars are displayed on one of the Maiolino et al. (2001) points.

The unusually low apparent gas-to-dust ratios for the four high X-ray S/N objects (#14-17) suggest that dust-reddening and X-ray absorption are not applicable in these cases. We therefore take the unusually low gas-to-dust ratios of these four sources to be another indicator of an intrinsically red continuum.

The ‘intrinsically red’ classification is shown in Figure 6, where we plot the gas/dust ratio, $N_{H,x}/E(B-V)_{spec}$, against the $\Delta(u-r) - \Delta(g-i)$ color. The vertical dotted line at $\Delta(u-r) - \Delta(g-i) = 0$ di-

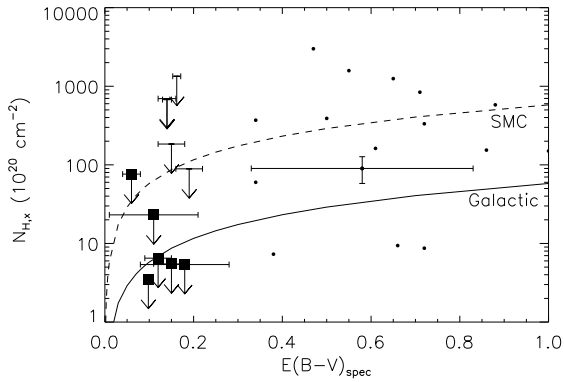


FIG. 5.— N_H (10^{20} cm^{-2}) vs. $E(B-V)_{\text{spec}}$ for the eleven quasars with X-ray $S/N > 4$. Because the N_H column is a 90% upper-limit for all of the quasars in the red sample, this results in an upper-limit on the gas/dust ratio. Sources classified as intrinsically red (§4.2) are marked with a solid circle. The Galactic (solid line) and SMC (dashed line) gas-to-dust ratios are plotted for reference. Points from Maiolino et al. (2001) are plotted as black points, with median error bars shown for one of these points.

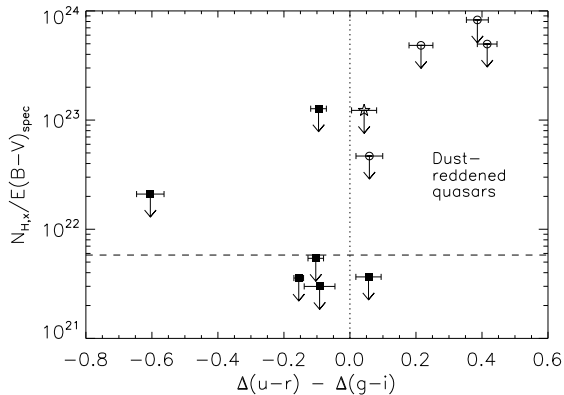


FIG. 6.— The gas/dust ratio, $N_{H,x}/E(B-V)_{\text{spec}}$, plotted against the $\Delta(u-r) - \Delta(g-i)$ color. The vertical dotted line at $\Delta(u-r) - \Delta(g-i) = 0$ divides the quasars with dust-reddened continuum shapes from the quasars with red power-law continua, as described in §3.4. The horizontal dashed line shows where the gas/dust ratio equals the Galactic value; sources below this line have unusually low gas/dust ratios and therefore are considered intrinsically red (§4.2). Sources ultimately classified as dust-reddened are plotted as open circles, while sources classified as intrinsically red are plotted as filled squares. The unclassified source (#10, §4.3) is plotted as a star.

vides the quasars with dust-reddened continuum shapes ($\Delta(u-r) - \Delta(g-i) > 0$) from the quasars with red power-law continua ($\Delta(u-r) - \Delta(g-i) < 0$), as discussed in §3.4. The horizontal dashed line shows where the gas/dust ratio equals the Galactic value. The sources in all but the top right quadrant are inconsistent with dust-reddening due to their low gas/dust ratios relative to the Galactic value and/or the lack of dust curvature in their optical continua.

Table 5 shows that the dust-reddened quasars are more likely to have the largest color excesses, while the intrinsically red quasars are more likely to have the smallest. This difference is significant in a K-S test at a probability of 1.7% that the two populations come from the same parent color distribution. This suggests that, while dust-reddening can occur to arbitrarily high values of $E(B-V)$, the intrinsic mechanism cannot steepen the continuum beyond a critical limit.

The mean optical slope of the intrinsically red quasar

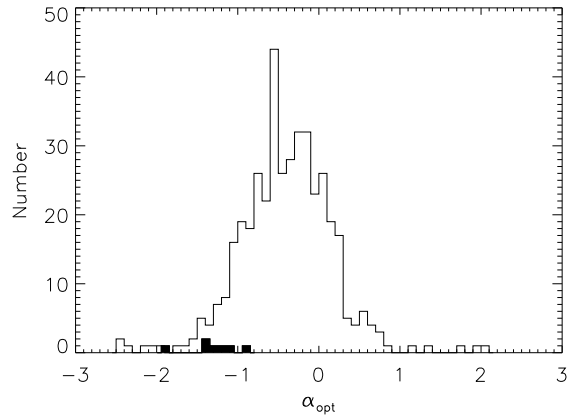


FIG. 7.— The optical spectral indices for the Large Bright Quasar Survey (Francis et al. 1991) are shown in an open histogram. Over-plotted is a solid histogram showing the optical spectral indices for the intrinsically red quasars.

candidates is $\langle \alpha_{\text{opt}} \rangle = -1.30$, where $F_\nu \propto \nu^\alpha$, with a dispersion $\sigma_{\alpha_{\text{opt}}} = 0.34$. Figure 7 shows a solid histogram of the optical slopes for the intrinsically red quasars, compared with an open histogram of the optical slopes for the Large Bright Quasar Survey (Francis et al. 1991). The intrinsically red quasars clearly lie in the red tail of the LBQS distribution. For comparison, the power-law obtained for the Vanden Berk composite SDSS quasar spectrum (2001) between 1300 and 5000 Å is $\alpha_{\text{opt}} = -0.44$.

4.3. Unclassified Quasars

The classification of two quasars is undetermined. SDSS J0232-0731 (#2) is X-ray weak ($\alpha_{\text{ox}} = -1.95$), but the signal is too weak to fit Γ or intrinsic absorption ($S/N = 3.23$). Dust-reddening is mild, and is significant only at 1.5σ ($E(B-V)_{\text{spec}} = 0.03 \pm 0.02$). However, the optical continuum shape is consistent with dust-type curvature (Table 5).

SDSS J2217-0812 (#10) is also ambiguous because, while it has normal Γ and $\alpha_{\text{ox,corr}}$ values ($\Gamma = 1.9_{-0.3}^{+0.4}$, $\alpha_{\text{ox,corr}} = -1.44$), the upper-limit on N_H is fairly high at $1.8 \times 10^{22} \text{ cm}^{-2}$, and the gas-to-dust ratio upper-limit is between the Galactic and SMC values. The optical continuum shape is consistent with both dust-reddened curvature and a red power-law within the photometric error bars on the relative colors. While absorption is not specifically indicated, it also cannot be ruled out.

4.4. Red Quasars and the $\alpha_{\text{ox}} - l_{\text{uv}}$ relation

Several studies (Avni & Tananbaum 1982; Vignali et al. 2003; Strateva et al. 2005; Steffen et al. 2006), have investigated an anticorrelation between α_{ox} and l_{uv} (the log of the 2500 Å luminosity) in radio-quiet quasars. Figure 4 (described in §3.2) shows that the majority of the sample is consistent with the Strateva et al. (2005, hereafter S05) $\alpha_{\text{ox}} - l_{\text{uv}}$ sample. Five sources, though, are X-ray weak, even after a correction for $E(B-V)_{\text{spec}}$ is applied, and appear inconsistent with the S05 $\alpha_{\text{ox}} - l_{\text{uv}}$ sample. All five have $S/N < 4$, so no correction can be made for N_H .

We have made a statistical comparison between the red quasar sample and the S05 sample. The S05 sample was selected from the SDSS using Data Release 2

photometry, so aside from updates to the SDSS quasar selection process between DR2 and DR3, the S05 quasar selection is the same as that of the red quasar sample, except for the red color cut. We simplified the comparison of the two samples by noting that the red sample luminosity is spread over a single decade, and for S05, α_{ox} changes by only 0.16 in this luminosity range. We thus restricted the luminosity range of both samples so that we could apply the one-dimensional Kolmogorov-Smirnov (K-S) test. The observed luminosity range of both the red quasar and the S05 samples are restricted to $l_{uv} = 29.4$ - 30.3 when comparing the uncorrected red quasar sample (Fig. 4, open circles) to the S05 sample. Since correcting α_{ox} for dust-reddening shifts the UV luminosity to a brighter interval, we restrict the luminosity range to $l_{uv} = 29.7$ - 30.8 when comparing the corrected red quasar sample (Fig. 4, filled circles) to the S05 sample. This excludes only one member of the red quasar sample (#17).

First we compare the complete red quasar sample (excluding the high l_{uv} source #17) with the S05 sample. We find a K-S probability of 0.02% that the two samples come from the same parent population. Next, we consider only the 11 sources for the K-S test where we were able to correct for X-ray absorption (i.e. $S/N > 4$, black circles in Fig. 4), so that we can compare the uncorrected and corrected α_{ox} - l_{uv} distributions to the S05 sample. Comparing first the uncorrected red quasar sample to the S05 sample, we find a probability of 10% that the two samples come from the same parent population. Then we compare the corrected red quasar sample to the S05 sample, and we find a K-S probability of 76%.

Six of 11 quasars with $S/N > 4$ are intrinsically red, so this suggests that intrinsically red quasars are not intrinsically X-ray weak compared to typical quasars, with the exception of SDSS J1002+0203 (#5). However, their peculiar SEDs make the physical interpretation unclear.

For sources with $S/N < 4$, it is plausible that correcting for absorption would significantly increase the K-S probability if the low S/N is due to large N_H columns. We find that if we apply a uniform correction to all of the low S/N quasars, an absorption column of $N_H > 10^{23} \text{ cm}^{-2}$ is required to achieve a K-S probability of at least 1% that the red quasar sample is drawn from the same parent population as the S05 sample.

4.5. X-ray Power-law Index

The mean X-ray photon index for sources with $S/N > 4$ is $\langle \Gamma \rangle = 1.58 \pm 0.09$, with an intrinsic dispersion $\sigma_\Gamma = 0.3$. Figure 8 plots Γ vs. S/N for each source with $S/N > 4$, with the mean Γ plotted as a solid line for reference, and the intrinsic dispersion plotted as dashed lines. For sources with multiple observations, the photon indices are averaged and the error plotted is the rms of the measured errors.

The mean Γ in this sample is flatter than that of other samples of quasar X-ray spectra including XMM-Newton samples. For example, Mateos et al. (2005) found a weighted mean $\langle \Gamma \rangle = 1.96 \pm 0.01$ with an intrinsic dispersion $\sigma_\Gamma = 0.4$ for 1137 serendipitously-selected XMM-Newton AGN. An investigation of 86 bright AGN detected in the XMM-Newton COSMOS field (Mainieri et al. 2007) gives $\langle \Gamma \rangle = 2.08 \pm 0.08$, with an intrinsic dis-

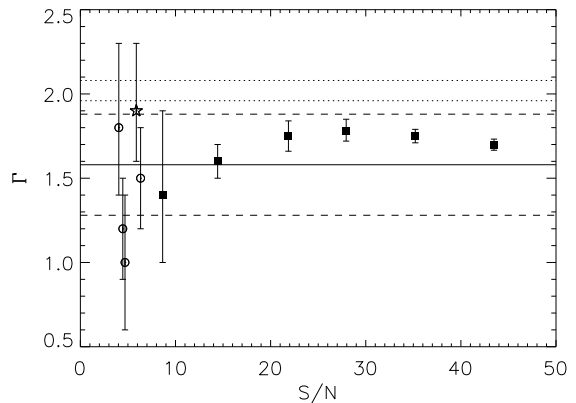


FIG. 8.— Best-fit X-ray spectral slope (Γ) vs. signal-to-noise. Objects classified as intrinsically red are marked as filled squares, while the dust-reddened objects are marked as open circles. The unclassified source (#10, §4.3) is plotted as a star. The average Γ and the intrinsic dispersion for the red sample are plotted as solid and dashed lines, respectively. The average Γ for the Mateos et al. (2005) sample ($\langle \Gamma \rangle = 1.86$) and the Mainieri et al. (2007) sample ($\langle \Gamma \rangle = 2.08$) are shown as dotted lines.

persion $\sigma_\Gamma = 0.24$. The two surveys are consistent within errors. These mean values are plotted as dotted lines for reference in Figure 8.

The measurement of N_H can affect the measurement of Γ . The contour plots in Figure 3 show that the two variables are correlated so that the same spectrum may be fit with a large N_H column and steep Γ , or with a smaller N_H column and flatter Γ . Therefore, the flatter mean Γ may be due to the effect of N_H on the X-ray spectra with lower S/N . Because the sources with higher X-ray S/N have tighter upper-limits, the Γ - N_H correlation is less noticeable for these sources (e.g. Fig. 3, #14, 15, 16, 17).

Considering only the intrinsically red group (squares in Fig. 8), excluding #5 due its low X-ray S/N , we find a mean $\Gamma = 1.66 \pm 0.08$, with an intrinsic dispersion of only $\sigma_\Gamma = 0.06$. This tight intrinsic dispersion shows that most of the variance in the intrinsically red group comes from measurement errors. Since the contour plots in Figure 3 show that Γ and N_H are not strongly correlated for any of the intrinsically red quasars, the flatter X-ray spectra cannot be explained by absorption.

A significantly flatter Γ may be explained via relation to other quantities. The X-ray spectral slope of normal quasars does not depend on optical luminosity or redshift (Shemmer et al. 2005; Vignali et al. 2005), but does depend slightly on X-ray luminosity (Dai et al. 2004; Saez et al. 2008). However, the Γ - L_x correlation contains too much intrinsic scatter (e.g. Figure 8 of Saez et al. 2008) to make conclusive statements about the intrinsically red quasars. The Γ - L_x correlation is not significant in the red quasar sample.

The strongest correlation reported between X-ray parameters and other variables is between Γ and the $H\beta$ emission-line FWHM, where flatter X-ray spectral slopes correlate with broader emission lines (Laor et al. 1997; Shemmer et al. 2006). The $H\beta$ emission line width is in turn believed to be anti-correlated with the accretion rate (Boroson & Green 1992; Brandt & Boller 1998). Narrow Line Seyfert 1's (NLS1) lie on one end of the Γ - $H\beta$ correlation, with steep X-ray spectral slopes, narrow $H\beta$ lines (Brandt & Boller 1998; Grupe 2004), and accre-

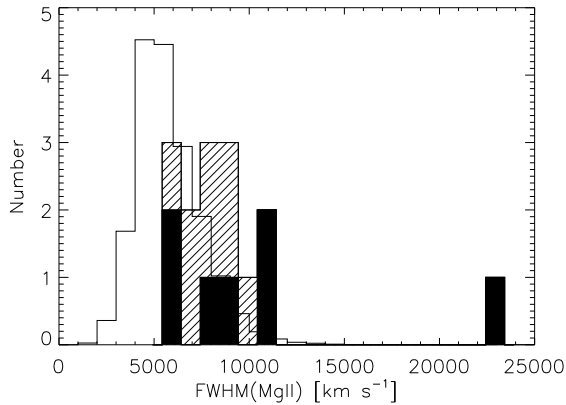


FIG. 9.— The histogram shows the MgII line widths (FWHM) of the full sample in Shen et al. (2007) (open histogram), the dust-reddened red quasars (line histogram), and the intrinsically red quasars (filled histogram).

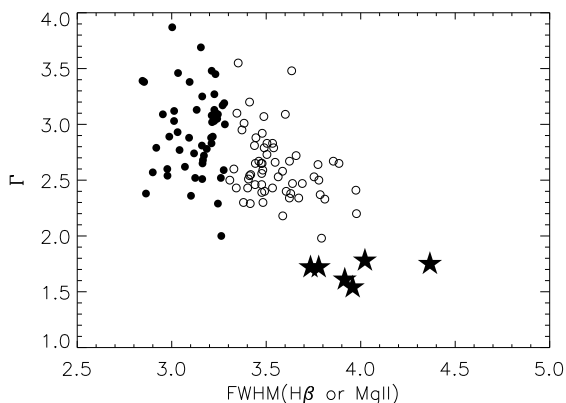


FIG. 10.— The well-known FWHM(H β - Γ) relation is shown, using the Grupe (2004) sample of Seyferts for reference. Broad-line Seyfert 1's are plotted as open circles and narrow-line Seyfert 1's are plotted as filled circles. For the red quasar sample, the width of the MgII line is plotted instead of the H β due to its availability and similarity to H β (§4.4). The intrinsically red quasars are plotted as filled stars. Γ is not well-determined for the absorbed quasars due to the high upper-limits on N_H , so we do not plot them on this plot.

tion rates close to the Eddington rate (Komossa 2007). While the H β line is not visible in the optical spectra for the red quasar sample, the broad MgII line is visible in all of the intrinsically red spectra and has an ionization potential similar to H β , and a FWHM that correlates well with FWHM(H β) (McLure & Jarvis 2002). The MgII line widths of all the red quasars are broader than average (Figure 9). This may be due to our color and redshift selection criteria, which biases the red quasar sample towards objects with strong MgII lines. However, the unabsorbed, flat X-ray spectral slopes combined with the broad MgII lines put the intrinsically red quasars on the correlation at the opposite end from NLS1's (Figure 10)¹³. NLS1's are believed to have accretion rates close to the Eddington rate because of their narrow H β lines and steep X-ray spectra (Komossa 2007). Steep red optical/UV continua seem to be an effective means of selecting this extreme population.

¹³ We do not plot the absorbed quasars on this plot because, due to the high N_H upper-limits, Γ is not well-determined for these objects.

4.6. Properties of Intrinsically Red Quasars

In this section, we investigate the basic properties of the intrinsically red quasars: their black hole masses (M_{BH}) and accretion rates (\dot{M}). These values, and the values from which they are derived, are listed in Table 12. The black hole masses are calculated by assuming virial motion of the broad-line clouds around the central black hole, an assumption justified from reverberation mapping (Peterson & Wandel 2000; Onken & Peterson 2002). The FWHM of the broad MgII line can then be used to determine the black hole mass using the following equation from McLure & Jarvis (2002):

$$\frac{M_{BH}}{M_{\odot}} = 3.37 \left(\frac{\lambda L_{3000}}{10^{37} W} \right)^{0.47} \left[\frac{FWHM(MgII)}{km s^{-1}} \right]^2$$

The luminosity at 3000 Å (L_{3000}) gives the radius of the BLR as determined by the R_{BLR} - L relation obtained from reverberation studies (e.g., Kaspi et al. 2000; Bentz et al. 2006). This relation was derived for a normal BBB-dominated SED. Since the BBB appears to be missing from the intrinsically red quasars, the ionizing continuum may be lower than normal; this would result in an overestimate of the black hole mass. Shang et al. (2005) show that the BBB peaks at ~ 1100 Å, so α_{ox} is a good estimate of the ionizing continuum. Since the intrinsically red quasars have α_{ox} values within the normal range (cf. Steffen et al. 2006), we can assume that the R_{BLR} - L relation is still valid for the intrinsically red quasars.

The apparent black hole masses for the intrinsically red quasars are relatively high, ranging from $\sim 10^9$ to $\sim 10^{10} M_{\odot}$ (cf. Shen et al. 2007).

We obtain the accretion rate from the bolometric luminosity: $L_{bol} = \eta \dot{M} c^2$. We assume an efficiency $\eta = 10\%$. Standard bolometric correction factors (e.g., Elvis et al. 1994; Kaspi et al. 2000) are not reliable for the intrinsically red quasars with their atypical SEDs. Instead, we integrated the optical power-law (α_{opt}) from 2,500 to 10,000 Å, the nominal UV-to-X-ray power-law (α_{ox}) from 2,500 Å to 2 keV, and the X-ray power-law (Γ) from 2-10 keV to give a rough approximation of the bolometric luminosity. Changing the break point between the two power-laws from 2500 Å to, e.g. 1150 Å (Shang et al. 2005), or even to 1000 Å, has a small effect on L_{bol} . Since object #17 is a lensed quasar, we reduce its luminosity by the modeled magnification factor, $M=15$ (Chartas 2000). Although we have no mid-IR data for these quasars, IR emission accounts for $\sim 40\%$ of the bolometric luminosity for a typical quasar SED (Richards et al. 2006). Therefore, if the intrinsically red quasars are similar, the IR emission will not change the total luminosity, and so the accretion rate, by more than a factor of a few. To constrain this estimate, we searched the IRAS Point Source Catalog and the Faint Source Catalog (FSC) for the red quasars, but found no matches. Sources in the FSC¹⁴ have flux densities greater than 200 mJy at 60 μ m, which gives an upper-limit to $\lambda L_{\lambda}(60 \mu m)/L_{bol} \lesssim 7.0$. This constrains the IR emission to be less than an order of magnitude of the bolometric luminosity. The estimated bolometric luminosities give a

¹⁴ <http://irsa.ipac.caltech.edu/IRASdocs/surveys/fsc.html>

TABLE 12
BLACK HOLE MASSES AND ACCRETION RATES OF INTRINSICALLY RED QUASARS

ID	SDSS name	FWHM(MgII) km s ⁻¹	M _{BH} 10 ⁹ M _⊙	L _{bol} 10 ⁴⁵ ergs s ⁻¹	M ^a M _⊙ yr ⁻¹	M/M _{Edd}
5	SDSS J1002+0203	10,800	9.1	2.5	0.5	0.002
12	SDSS J1133+4900	9,100	3.3	4.2	0.7	0.010
13	SDSS J1254+5649	8,200	0.68	1.6	0.3	0.019
14	SDSS J0959+0209	23,200	9.9	1.6	0.3	0.001
15	SDSS J0958+0213	10,500	1.3	2.5	0.5	0.015
16	SDSS J1053+5735	5,400	0.76	3.4	0.6	0.035
17	SDSS J0913+5259	6,000	3.9	2.6	0.5	0.005

^aThe accretion rate calculated from $L_{bol} = \eta \dot{M} c^2$, where $\eta = 0.1$.

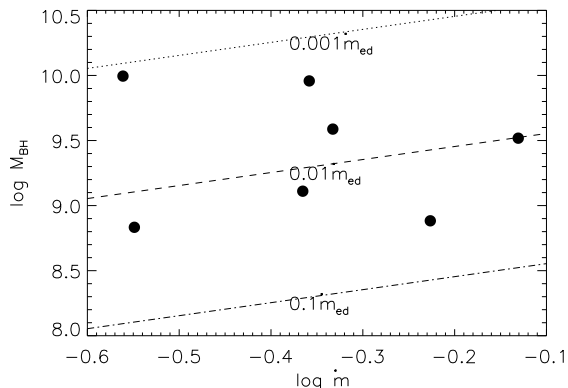


FIG. 11.— Black hole mass (M_{\odot}) is plotted against the accretion rate ($M_{\odot} \text{ yr}^{-1}$). The Eddington accretion rate is plotted for a reference as a solid line, while correspondingly smaller fractions of the Eddington luminosity are plotted as dash-dotted, dashed, and dotted lines respectively, as labeled in the plot.

lower bolometric correction compared to previous work. $L_{bol}/\lambda L_{3000} = 2.6 \pm 1.6$ for the intrinsically red sample, a factor 2.4 lower than that obtained by Elvis et al. (1994) (6.3 ± 3.1).

Using L_{bol} , we find that the intrinsically red quasars have relatively low accretion rates (Figure 11). The intrinsically red quasars lie clustered between ~ 0.001 - $0.03 \dot{M}_{Edd}$. In comparison, typical accretion rates for optically or UV-selected quasars range from $\dot{M}/\dot{M}_{Edd} \sim 0.03$ - 10.0 , with a median value of ~ 0.6 (Warner, Hamann & Dietrich 2004; Bonning et al. 2007). The low accretion rates of the intrinsically red quasars are in agreement with their position on the Γ -FWHM(MgII) correlation (Fig. 10, §4.5)

5. INTRINSICALLY RED QUASARS: PHYSICAL MODELS

We have found a substantial subset of red quasars whose red colors are probably due to intrinsically red optical emission in the optical/UV rather than dust-reddening. This subset comprises a large fraction ($7/17 \sim 40\%$) of SDSS quasars with $(g-r) \geq 0.5$. Note that this is based on color selection; selection via relative colors (e.g. $\Delta(g-i) > 0.35$) would likely change the frequency of intrinsically red quasars because dust-reddened quasars have a redder color distribution than intrinsically red quasars (§4.2). For redshifts $z \sim 1$ - 1.5 , the Small Blue Bump reddens the observed $g-r$ colors resulting in similar samples, whether selected by color or color excess. However, for redshifts $z \sim 1.5$ - 2 , the $g-r$ color decreases; for this range, selection via color excess would increase the number of quasars with smaller color excesses, thereby possibly increasing the fraction of in-

trinsically red quasars.

Quasars with intrinsically red SEDs have been discussed before (e.g., Risaliti et al. 2003; Hall et al. 2006, see §1). For example, the intrinsically red quasars found by Hall et al. (2006) do not show absorption in the optical or X-ray continua, yet they also have steep optical slopes ($\langle \alpha_{opt} \rangle = -1.0$, $\sigma_{\alpha_{opt}} = 0.2$), determined via fits to the SDSS spectra.

Intrinsically steep optical power-laws suggest that these quasars have a different continuum emission mechanism from ordinary quasars. We consider 3 possibilities to explain the red optical power-laws: (1) strong synchrotron emission visible in the optical, (2) a high-temperature BBB, which exposes the red power-law that may underlie typical optical emission, or (3) a low-temperature BBB resulting from a low accretion rate, such that the steep, high-energy tail of the BBB is visible in the optical.

5.1. Synchrotron Emission

Synchrotron radiation could result in a red optical power-law. However, typical synchrotron emission can be discounted for two reasons. First, synchrotron radiation is strongest in the radio, with a turnover frequency at $\nu_m = 10^{11}$ Hz (Marscher 1995). Therefore, we would expect strong radio emission in all of the intrinsically red quasars, when in fact only one can be classified as radio-loud (Table 1). Second, even if a higher than normal turnover frequency allowed the synchrotron emission to dominate in the optical, the superposition of synchrotron emission on a BBB would result in a ‘U’-shaped spectrum (Fig. 2 of Francis et al. 2000). This is not observed in any of the optical spectra.

5.2. Exposed Underlying Power-law

A red power-law is sometimes proposed to underlie the BBB in other quasars (Malkan & Sargent 1982; Ward et al. 1987; Lawrence 2005). If the BBB were removed or diminished, this underlying power-law would be exposed. One way of ‘removing’ the BBB is to shift it to higher temperatures. Possible examples of high-temperature BBB’s exposing a red, underlying optical power-law are known: the narrow-line Seyfert 1 galaxies RE J1034+396 (Puchnarewicz et al. 1995a) and RE J2248-511 (Puchnarewicz et al. 1995b). In these objects, the optical power-law slopes are -1.3 and -0.9 , respectively. RE J1034+396 is an EUV-selected source with an ultrasoft X-ray excess that peaks near 0.4 keV. The effective maximum temperature of the accretion disk is $T \sim 10^6$ K ($\log \nu_{max} \sim 16.8$), more than an order of magnitude hotter than typical quasar accretion disk temper-

atures ($T \sim 10^{4.5}$ K, $\log \nu_{max} \sim 15.3$, Malkan & Sargent 1982). The optical spectrum of this source shows no signs of a BBB. RE J2248-511 also has a high-energy turnover at around 0.25 keV, but a blackbody is a poor fit to the X-ray data.

The presence of an underlying power-law may be explained by weak synchrotron emission from an associated jet emitting at a large angle to the line of sight. This synchrotron emission would necessarily be weak for a radio-quiet object, which is why the BBB must be removed or otherwise modified in order for the red power-law to be visible in the optical. Alternatively, unsaturated Comptonization of a seed spectrum can produce a power-law over seven decades in frequency (e.g., Maraschi, Treves & Roasio 1982).

Assuming a simple model of the accretion disk as a sum of blackbodies, Lawrence (2005) showed that quasar SEDs scale homologously with temperature, such that hotter AGN have thermal peaks at higher frequencies. If the local temperature of the disk is due to the release of the gravitational binding energy, then the temperature of the accretion disk scales homologously with the accretion rate. Since the M_{BH} determines the inner radius of the accretion disk, scaling with black hole mass is model-dependent and non-homologous; however, simple models show that a less massive black hole will have a hotter maximum effective disk temperature (Lawrence 2005). Therefore, high accretion rates and/or low black hole masses could shift the BBB to higher temperatures/energies.

Neither high accretion rates nor low black hole masses are observed in the intrinsically red quasars (§4.6), but since the SDSS/XMM red quasars have relatively high redshifts ($z \sim 1-2$), a soft X-ray turnover similar to that found in the Puchnarewicz et al. (1995a,b) objects would be shifted to $\sim 0.4 \text{ keV}/(1+z) = 0.1-0.2 \text{ keV}$. This turnover would lie below the observed XMM-EPIC energy band (0.5-10 keV). A hidden BBB in the EUV or soft X-rays would increase the bolometric luminosity, thereby increasing the accretion rates. However, an increase in the ionizing continuum would mean that the black hole mass calculations are underestimates. Since the effective maximum disk temperature goes roughly as $T \propto (\dot{M}^{1/4} M_{BH}^{-1/2})$, a NLS1 ($\langle M_{BH} \rangle \sim 10^6 - 10^7 M_{\odot}$, Grupe & Mathur 2004) can achieve an effective maximum disk temperature of 10^6 K at normal accretion rates, but highly super-Eddington conditions ($L/L_{Edd} \sim 10^3$) are required for a quasar with $M_{BH} \sim 10^9 M_{\odot}$ to reach the same temperature. If the black hole masses are underestimates, then even higher accretion rates are required. Therefore, a high-temperature BBB is unlikely to explain the intrinsically red quasars.

5.3. The Tail of a Low-Temperature Big Blue Bump

Low disk temperatures due to low accretion rates and/or large black hole masses should shift the peak of the Big Blue Bump to longer, near-infrared wavelengths (Frank, King & Raine 2002, p. 90). Our bolometric luminosity estimates for the intrinsically red quasars suggest accretion rates $\sim 10-100$ times lower than typical quasars (Fig. 11, §4.6). The low accretion rate hypothesis is supported by the uniformly flat X-ray spectral slopes and broad MgII lines of the intrinsically red

quasars (Fig. 10, §4.5). We can determine the temperature of the thermal peak expected for the calculated accretion rate using the scaling relation developed by Lawrence (2005). A typical quasar has an effective maximum temperature $\sim 10^{4.8}$ K (Malkan & Sargent 1982); this corresponds to a BBB peak at $\log \nu_{max} \sim 15.6$.

Assuming a conservative accretion rate of $0.1 M_{Edd}$ for the Elvis et al. (1994) SED, an intrinsically red quasar accreting at a rate lower by a factor 10 will be a factor of $(10)^{1/4} \sim 1.8$ lower in temperature, so the BBB will peak at $\log \nu_{max} \sim 15.3$. The most extreme accretion rate ($0.001 M_{Edd}$, #14) gives a BBB peak at $\log \nu_{max} \sim 15.1$.

We can model the low disk temperature expected from a low accretion rate using a simple template SED. The CLOUDY package approximates the AGN SED with a toy model (Ferland 2001):

$$F_{\nu} = A\nu^{-\alpha_{uv}} e^{-h\nu/kT_{cut}} + B\nu^{\alpha_x}$$

The A and B constants are normalizations for the optical/UV and X-ray terms, respectively. The UV and X-ray slopes are power-laws (α_{uv} and α_x), where $F_{\nu} \propto \nu^{\alpha}$. The high-energy cut-off, kT_{cut} , corresponds to the maximum accretion disk temperature. We performed a qualitative fit, first to the Elvis et al. (1994) SED, and then to the intrinsically red quasar SED. For the Elvis et al. (1994) SED, we use $\alpha_{uv} = -0.5$, $\alpha_x = -1$, and $T_{cut} = 10^{4.8}$ K. For the intrinsically red SEDs, we change α_x to the value obtained in the X-ray fit, and we change T_{cut} by the amount expected for the lower accretion rate, calculated according to the Lawrence (2005) scaling relation. Since the UV power-law defines the rise of the BBB, we do not change α_{uv} . Figure 12 shows the SED data and model fit for all seven intrinsically red quasars. The figure demonstrates that a lower disk temperature qualitatively reproduces the observed red power-law for four objects. Two objects (#15 and #16) are better fit with a an accretion rate an order of magnitude smaller than that shown. A third object (#5) is not fit well by any model.

6. CONCLUSIONS AND FUTURE WORK

We have cross-correlated the SDSS DR3 Quasar Catalog (Schneider et al. 2005) with the XMM-Newton archive, selecting the reddest ($g - r \geq 0.5$), moderate-redshift ($0.9 < z < 2.1$) quasars. We obtain a sample of 17 quasars, 16 of which are detected in the X-rays. Using both optical and X-ray data to constrain dust-reddening and absorption allowed us to distinguish between obscured and intrinsically red quasars, although two cases remain ambiguous.

Eight quasars are dust-reddened in the optical and, while the X-ray data prefer an unabsorbed power-law, the upper-limits are high enough that X-ray absorption at the level expected for an SMC dust-to-gas ratio is allowed. For the three quasars with high enough X-ray S/N to fit a power-law + intrinsic absorption model, we obtain upper-limits of $3 - 13 \times 10^{22} \text{ cm}^{-2}$. For five sources, the X-ray S/N is too low to fit spectral models. However we can obtain a lower-limit to N_H by comparing the $\alpha_{ox} - l_{uv}$ distribution of the red quasar sample to that of Strateva et al. (2005), a recent study that uses a similar selection method, aside from the red color cut. If the two samples come from the same parent distribution,

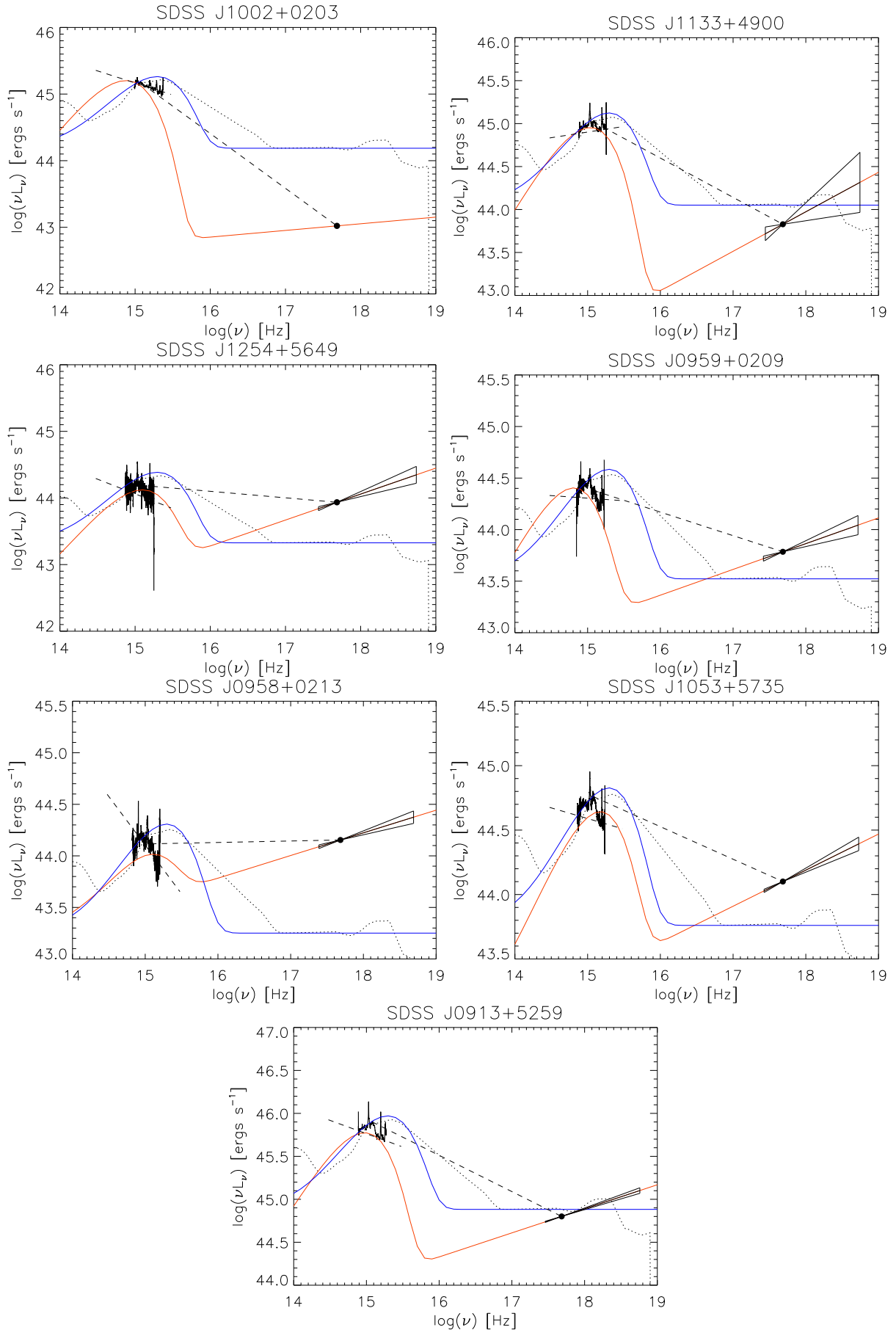


FIG. 12.— The SED is plotted as a solid black line for the intrinsically red sources #5, #12–#17, starting with #5 in the top left panel. Units are $\log(\nu L_\nu)$ [ergs s^{-1}] vs. $\log(\nu)$ [Hz]. The Elvis et al. (1994) SED is overplotted for reference as a dotted black line. A toy SED model employing a simple ‘disk’ shape and parameters as described in §5.3 is overplotted as a solid, blue line to match the Elvis et al. (1994) SED. A second toy model is calculated, where all the parameters remain the same except that the cut-off temperature is reduced by the amount expected from the calculated accretion rate (§5.3). This second model is overplotted as a solid, red line. The optical power-law (α_{opt}) and the optical-to-X-ray power-law (α_{ox}) are overplotted as dashed lines. 90% errors on the X-ray power-law are plotted as a bow

an absorbing column of at least 10^{23} cm^{-2} is required for the five red quasars.

Seven quasars display no evidence of X-ray absorption, and dust-reddening is contraindicated by the continuum shape as determined by the optical photometry. These quasars seem to form a group with intrinsically red power-laws in the optical/UV. It seems that these intrinsically red power-laws may be caused by lower accretion rates: low accretion rates are derived from M_{BH} and L_{bol} estimates, although the M_{BH} values may be biased high by the red SED's. Moreover the unusually broad MgII emission lines place these quasars on the Γ -FWHM(MgII) relation, also suggesting lower accretion rates.

The intrinsically red quasars are a substantial population with extreme characteristics that are well-suited to X-ray follow-up. Since 7 intrinsically red quasar candidates have been found in the 1% of the SDSS DR3 quasar catalog that overlaps with archival XMM-Newton observations, as many as 700 intrinsically red candidates may exist in the complete catalog. Since the DR6 has more than doubled the number of SDSS quasars, we can expect 1600 intrinsically red quasar candidates, 16 of which have been observed serendipitously with the XMM-Newton. The intrinsically red quasar candidates in this paper also merit further observations in order to confirm the lack of dust-reddening and pinpoint the physical cause of the red optical power-laws. For example, NIR (e.g. JHK) spectra would include $H\alpha$ and $H\beta$, and so could give an independent measure of dust-reddening via the Balmer

decrement. NIR measurements will also constrain a low-temperature disk model, as well as L_{bol} and so \dot{M} . With optical and X-ray spectra already available, the intrinsically red quasar candidates described in this paper are well-suited to more complex SED modeling.

The authors thank Gordon Richards for his help in navigating the SDSS database, Joanna Kuraszkiwicz for her help with understanding IRAF, and Bożena Czerny for helpful conversations regarding SED models. We also thank the anonymous referee for helpful comments which improved the presentation of this work. This paper is based on observations obtained with XMM-Newton, an ESA science mission with instruments and contributions directly funded by ESA Member States and NASA, and the Sloan Digital Sky Survey (SDSS). Funding for the SDSS and SDSS-II has been provided by the Alfred P. Sloan Foundation, the Participating Institutions, the National Science Foundation, the U.S. Department of Energy, the National Aeronautics and Space Administration, the Japanese Monbukagakusho, the Max Planck Society, and the Higher Education Funding Council for England. This research also made use of the NASA/IPAC Infrared Science Archive, which is operated by the Jet Propulsion Laboratory, California Institute of Technology, under contract with the National Aeronautics and Space Administration. This work has been partially funded by NASA Grants NASA NNX07AI22G and NASA GO6-7102X G06-7102X.

REFERENCES

- Abazajian K. et al. 2005, *AJ*, 129, 1755
 Avni Y. & Tananbaum H. 1982, *ApJ*, 262, L17 & Green R.F. 1987, *ApJ*, 314, 699
 Bentz M., Peterson B.M., Pogge R.W., Vestergaard M. & Onken C.A. 2006, *ApJ*, 644, 133
 Bohlin R.C., Savage B.D., Drake J.F. 1978, *ApJ*, 224, 132
 Bonning E.W., Cheng L., Shields G.A., Salvander S. & Gebhardt K. 2007, *ApJ*, 659, 211
 Boroson, T. A., & Green, R. F. 1992, *ApJS*, 80, 109
 Brandt, N., & Boller, T. 1998, *Astron. Nachr.*, 319, 163
 Brotherton, M. S., Tran, H. D., Becker, R. H., Gregg, M. D., Laurent-Muehleisen, S. A. & White, R. L. 2001, *ApJ*, 546, 775
 Chartas G. 2000, *ApJ*, 531, 81
 Croom S.M., Smith R.J., Boyle B.J., Shanks T., Miller L., Outram P.J. & Loaring N.S. 2004, *MNRAS*, 349, 1397
 Cutri, R.M., Nelson, B.O., Francis, P.J., & Smith, P.S. 2002, *ASPC*, 284, 187
 Czerny B., Li J., Loska Z. & Szczerba R. 2004, *MNRAS*, 348, L54
 Dai X., Chartas G., Eracleous M. & Garmire G.P. 2004, *ApJ*, 605, 45
 Elvis M. et al. 1994, *ApJ*, 95, 1
 Ferland, G. J. 2001, *Hazy, a Brief Introduction to CLOUDY 96.00*, Univ. Kentucky Dept. Phys. Astron. Int. Rep. (Lexington: Univ. Kentucky)
 Francis J.F., Hewett P.C., Foltz C.B., Chaffee F.H., Weymann R.J. & Morris S.L. 1991, *ApJ*, 373, 465
 Francis P.J., Whiting M.T. & Webster, R.L. 2000, *PASA*, 2000, 53, 56
 Frank J., King A. & Raine D.J. 2002, *Accretion Power in Astrophysics*, 3rd edition, Cambridge University Press
 Gordon K., Clayton G., Misselt K.A., Landolt A. & Wolff M. 2003, *ApJ*, 594, 279
 Green P. & Mathur S. 1996, *ApJ*, 462, 637
 Green P., Aldcroft T., Mathur S., Wilkes B. & Elvis M. 2001, *ApJ*, 558, 109
 Grupe D. 2004, *AJ*, 127, 1799
 Grupe D. & Mathur S. 2004, *ApJ*, 606, L41
 Hall P. et al. 2006, *AJ*, 132, 1977
 Hopkins P. et al. 2004, *ApJ*, 128, 1112
 Issa M., MacLaren I. & Wolfendale A. 1990, *A&A*, 236, 237
 Kaspi S., Smith P.S., Netzer H., Maoz D., Jannuzi B.T. & Giveon U. 2000, *ApJ*, 533, 631
 Kellerman K., Sramek R., Schmidt M., Shaffer D. & Green R. 1989, *AJ*, 98, 4
 Kent S.M., Dame T.M. & Fazio G. 1991, *ApJ*, 378, 131
 Komossa S. *astroph/0710.3326K*
 Kuhn O., Elvis M., Bechtold J. & Elston R. 2001, *ApJS*, 136, 225
 Laor A., Fiore F., Elvis M., Wilkes B.J. & McDowell J.C. 1997, *ApJ*, 477, 93
 Lawrence A. 2005, *MNRAS*, 363, 57
 McLure R.J. & Jarvis M.J. 2002, *MNRAS*, 337, 109
 Maccacaro T. & Perola G. C. 1981, *ApJ*, 246, L11
 Mainieri et al. 2007, *ApJ*, 172, 368
 Maiolino R., Marconi A., Salvati M., Risaliti G., Severgnini E.O., La Franca F. & Vanzli L. 2001, *A&A*, 365, 28
 Malkan M. & Sargent W. 1982, *ApJ*, 254, 22
 Maraschi L., Treves A. & Roasio R. 1982, *ApJ*, 253, 312
 Marscher A.P. 1995, *PNAS*, 92, 11439
 Mateos et al. 2005, *A&A*, 433, 855
 Mathur S., Elvis M. & Singh K. 1995, *ApJ*, 455, L9
 Nousek J.A. & Shue D.R. 1989, *ApJ*, 342, 1207
 Onken C. & Peterson B.M. 2002, *ApJ*, 572, 746
 Peterson B.M. & Wandel A. 2000, *ApJ*, 540, L13
 Pitman K., Clayton G.C. & Gordon K.D. 2000, *PASP*, 112, 537
 Prevot M., Lequeux J., Maurice E., Prevot L. & Rocca-Volmerange B. 1984, *A&A*, 132, 389
 Puchnarewicz E.M., Mason K.O., Siemiginowska A & Pounds K.A. 1995a, *MNRAS*, 276, 20
 Puchnarewicz E.M., Branduardi-Raymont G., Mason K.O. & Sekiguchi K. 1995b, *MNRAS*, 276, 1281
 Reichard T. A. et al. 2003, *AJ*, 125, 1711
 Richards et al. 2002, *AJ*, 123, 2945
 Richards et al. 2003, *AJ*, 126, 1131
 Richards et al. 2006, *ApJ*, 166, 470
 Risaliti G. & Elvis M. 2005, *ApJ*, 629, L17
 Risaliti G., Elvis M., Gilli R. & Salvati M. 2003, *ApJ*, 587, L9

- Saez C. et al. 2008, *astroph/08013599v1*
Schmidt M. & Green R.F. 1983, *ApJ*, 269, 352
Schneider et al. 2005, *AJ*, 130, 367
Serjeant S. & Rawlings S. 1996, *Nature*, 379, 304
Shang Z. et al. 2005, *ApJ*, 619, 41
Shemmer O., Brandt W.N., Netzer H., Maiolino R. & Kaspi S. 2006, *ApJ*, 646, L29
Shemmer et al. 2005, *ApJ*, 630, 729
Shen Y., Greene J., Strauss M., Richards G. & Schneider D. 2007, *astroph/0709.3098v2*
Smith P.S., Schmidt G.D., Hines D.C., Cutri R.M. & Nelson B.O. 2002, *ApJ*, 569, 23
Steffen A., Strateva I., Brandt W., Alexander D., Koekemoer A., Lehmer B., Schneider D. & Vignali C. 2006, *AJ*, 131, 2826
Strateva I.V., Brandt W.N., Schneider D.P., Vanden Berk D.G. & Vignali C. 2005, *ApJ*, 130, 387
Strueder L. et al. 2001, *A&A*, 365, L18
Tananbaum H. et al. 1979, *ApJ*, 234, L9
Tolea, A., Krolik, J. H., Tsvetanov, Z. 2002, *ApJ*, 578, L31
Tucker W. H., 1975, *Radiation Processes in Astrophysics*. Wiley, New York
Turner M. et al. 2001, *A&A*, 365, L27
Urrutia T., Lacy M., Gregg M.D. & Becker R.H. 2005, *ApJ*, 627, 75
Vanden Berk D.E. et al. 2001, *AJ*, 122, 549
Vignali C., Brandt W.N. & Schneider D.P. 2002, *AJ*, 125, 443
Vignali C., Brandt W.N., Schneider D.P. & Kaspi S. 2005, *AJ*, 129, 2519
Voit G.M., Wemann R.J. & Korista K.T. 1993, *ApJ*, 413, 95
Ward M.J., Elvis M., Fabbiano G., Carleton N.P., Willner S.P. & Lawrence A. 1987, *ApJ*, 315, 74
Warner C., Hamann F. & Dietrich M. 2004, *ApJ*, 608, 136
Webster R., Francis P.J., Peterson B.A., Drinkwater M.J. & Masci, F.J. 1995, *Nature*, 375, 469
White R., Becker R., Helfand D. & Gregg M. 1997, *ApJ*, 475, 479
Whiting M.T., Webster R.L. & Francis P.J. 2000, *MNRAS*, 323, 718
Wilkes B.J., Schmidt G.D., Cutri R.M., Ghosh, H., Hines D.C., Nelson B. & Smith P.S. 2002, *ApJ*, 564, L65
Wilkes B.J., Pounds K.A., Schmidt G.D., Smith P.S., Cutri R.M., Ghosh H., Nelson B. & Hines D.C. 2005, *ApJ*, 634, 183
Wills B.J., Netzer H. & Wills D. 1985, *ApJ*, 288, 94
Yamamoto T. M. & Vasevicius V. 1999, *PASJ*, 51, 405